



HHS Public Access

Author manuscript

Cell Rep. Author manuscript; available in PMC 2021 May 21.

Published in final edited form as:

Cell Rep. 2021 April 20; 35(3): 109008. doi:10.1016/j.celrep.2021.109008.

Alzheimer's pathology causes impaired inhibitory connections and reactivation of spatial codes during spatial navigation

Stephanie M. Prince^{1,2}, Abigail L. Paulson¹, Nuri Jeong^{1,2}, Lu Zhang¹, Solange Amigues¹, Annabelle C. Singer^{1,3,*}

¹Coulter Department of Biomedical Engineering, Emory University and Georgia Institute of Technology, Atlanta, GA 30332, USA

²Neuroscience Graduate Program, Graduate Division of Biological and Biomedical Sciences, Emory University, Atlanta, GA, 30322, USA

³Lead contact

SUMMARY

Synapse loss and altered synaptic strength are thought to underlie cognitive impairment in Alzheimer's disease (AD) by disrupting neural activity essential for memory. While synaptic dysfunction in AD has been well characterized in anesthetized animals and *in vitro*, it remains unknown how synaptic transmission is altered during behavior. By measuring synaptic efficacy as mice navigate in a virtual reality task, we find deficits in interneuron connection strength onto pyramidal cells in hippocampal CA1 in the *5XFAD* mouse model of AD. These inhibitory synaptic deficits are most pronounced during sharp-wave ripples, network oscillations important for memory that require inhibition. Indeed, *5XFAD* mice exhibit fewer and shorter sharp-wave ripples with impaired place cell reactivation. By showing inhibitory synaptic dysfunction in *5XFAD* mice during spatial navigation behavior and suggesting a synaptic mechanism underlying deficits in network activity essential for memory, this work bridges the gap between synaptic and neural activity deficits in AD.

Graphical abstract

This is an open access article under the CC BY-NC-ND license (<http://creativecommons.org/licenses/by-nc-nd/4.0/>).

*Correspondence: asinger@gatech.edu.

AUTHOR CONTRIBUTIONS

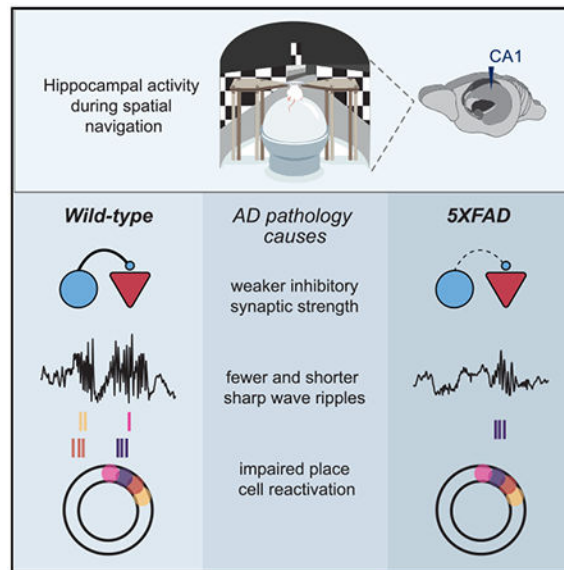
Conceptualization, S.M.P., A.C.S., and A.L.P.; methodology, S.M.P., A.C.S., and A.L.P.; investigation, S.M.P., A.C.S., A.L.P., S.A., and N.J.; formal analysis, S.M.P., A.C.S., and L.Z.; data curation, S.M.P.; writing – original draft, S.M.P. and A.C.S.; writing – review & editing, S.M.P., A.C.S., A.L.P., N.J., and L.Z.; visualization, S.M.P. and A.C.S.; funding acquisition, A.C.S.; supervision, A.C.S.

SUPPLEMENTAL INFORMATION

Supplemental information can be found online at <https://doi.org/10.1016/j.celrep.2021.109008>.

DECLARATION OF INTERESTS

The authors declare no competing interests.



In brief

Prince et al. find impaired inhibitory synapses, sharp-wave ripples, and place cell reactivation during behavior in a mouse model of Alzheimer's disease. These results link synaptic deficits in Alzheimer's disease to dysfunction of neural activity essential for memory.

INTRODUCTION

Alzheimer's disease (AD) is the most common form of dementia and is associated with neural dysfunction from the level of synapses to networks. Synaptic dysfunction is thought to be key to the pathogenesis of AD because synaptic loss is one of the best correlates of cognitive impairment in the disease (DeKosky and Scheff, 1990; Selkoe, 2002; Terry, 2000; Terry et al., 1991). Several studies have shown that amyloid beta, one of the pathogenic proteins that accumulate in AD, affects synaptic transmission (Abramov et al., 2009; Bero et al., 2011; Chapman et al., 1999; Freir et al., 2001; Hsia et al., 1999; Puzzo et al., 2008; Stéhan et al., 2001; Walsh et al., 2002). Taken together, these findings have led to the hypothesis that elevated levels of amyloid beta cause synaptic dysfunction, which disrupts neural activity essential for memory and ultimately leads to cognitive decline (Palop and Mucke, 2010). However, prior work examining synaptic dysfunction in animal models of AD was conducted *in vitro* or in anesthetized animals; these prior studies have not investigated synaptic changes in awake, behaving animals. Neural activity is much less dynamic in anesthetized animals (Constantinople and Bruno, 2011; Steriade et al., 2001), and anesthesia drastically alters synaptic excitation and inhibition (Haider et al., 2013). Thus, because amyloid beta influences synaptic transmission and is influenced by neural activity, it is important to study synaptic function in AD in awake animals during behavior.

Synaptic activity alterations caused by AD pathology are thought to disrupt neural activity that is essential for memory. In the *5XFAD* mouse model, a well-established amyloid model of AD with five human familial AD mutations (Oakley et al., 2006), synaptic loss increases

with age, and synaptic transmission *in vitro* is correlated with memory deficits (Kimura and Ohno, 2009; Oakley et al., 2006). *5XFAD* and *apoE4* mouse models display a decreased abundance of sharp-wave ripple (SWR) events in the hippocampus (Gillespie et al., 2016; Iaccarino et al., 2016; Jones et al., 2019). These SWRs, high-frequency oscillations accompanied with bursts of population activity, are of particular interest because they are important for cognitive processes such as learning and memory (Buzsáki, 2015; Carr et al., 2011; Girardeau et al., 2009; Girardeau and Zugaro, 2011; Jadhav et al., 2012; Pfeiffer and Foster, 2013; Singer et al., 2013), and they are generated in the hippocampus, one of the first regions affected in AD (Braak and Braak, 1991). Several studies have shown disrupted synapses *in vitro* or in post-mortem tissue, as well as deficits in neural activity associated with memory (Leung et al., 2012; Li et al., 2009). It is thought that these synaptic deficits lead to deficits in neural activity because excitatory and inhibitory interactions are important for generating the neural activity that is lacking in AD, such as SWR events. However, it remains unknown how synaptic activity is disrupted in awake, behaving animals, whether excitatory or inhibitory disruptions predominate, and whether synaptic deficits occur during patterns of abnormal neural activity, such as SWRs.

Given the hypothesized role of synaptic dysfunction in AD, we asked whether excitatory and inhibitory synaptic connections were disrupted in an awake, behaving mouse model of AD. We hypothesized that *5XFAD* mice would have deficits in excitatory and inhibitory synaptic transmission based on prior work showing spine density loss of pyramidal cells in post-mortem tissue of *5XFAD* mice and interneuron vulnerability in multiple mouse models of AD (Crowe and Ellis-Davies, 2014; Leung et al., 2012; Li et al., 2009; Palop et al., 2007; de Pins et al., 2019; Verret et al., 2012). We aimed to study neural activity in awake, behaving animals at an age when both behavioral and synaptic deficits were clearly present, and thus we examined neural and synaptic deficits in older *5XFAD* mice (Buskila et al., 2013; Oakley et al., 2006). We recorded spiking activity from many single neurons in CA1 simultaneously as animals licked for reward in a circular track. We show deficits in the connection strength of interneuron inhibition onto pyramidal cells in *5XFAD* mice during behavior, and these deficits are most pronounced during SWRs. Because interactions between interneurons and pyramidal cells play a key role in SWR generation and maintenance and SWRs are essential for spatial memory, we thought SWR activity might also be affected (Alger and Nicoll, 1982; Buzsáki, 1986; Buzsáki et al., 1983; Csicsvari et al., 1999; Klausberger et al., 2003; Pouille and Scanziani, 2001; Stark et al., 2014; Ylinen et al., 1995). We found deficits in the abundance, duration, and amplitude of SWR activity in *5XFAD* mice. Lastly, we show that place cells in *5XFAD* mice had impaired reactivation during SWRs compared to wild-type (WT) littermates. These results reveal *in vivo* deficits from the level of synapses to neural codes essential for learning and memory in the *5XFAD* mouse model of AD and show that these deficits are most pronounced during SWRs, which are essential for spatial learning and memory. This work bridges gaps between synaptic dysfunction and neural activity essential for memory and thus reveals how AD pathology leads to disruption across multiple scales in memory circuits.

RESULTS

5XFAD mice and WT littermates lick for reward in a virtual reality spatial task

To investigate altered synaptic efficacy and electrophysiological activity during behavior, we designed a virtual reality (VR) spatial navigation task to record neural activity as older *5XFAD* mice and their WT littermates navigated through an environment (Figure 1A). At this age, *5XFAD* mice have well-established deficits in memory performance (Martorell et al., 2019; Oakley et al., 2006). However, in these behavioral tasks, the impaired animals sample the environment differently than do intact animals, and thus neural activity during these behaviors is confounded by the animals' differences in sampling. Therefore, we characterized neural activity deficits in a simple task that both *5XFAD* mice and their WT littermates sampled similarly, as has been done often in studies comparing neural activity in transgenic and WT mice with behavioral differences (e.g., Dragoi and Tonegawa, 2013; Suh et al., 2013). Animals were trained to lick at specific locations of a circular track in order to receive a reward of sweetened condensed milk (Figures 1B and S1A). We quantified behavioral metrics important to hippocampal neural activity, including velocity and licking, and found that animals of both genotypes licked in order to trigger a reward early in the reward zone (see STAR Methods; Figures 1C and S1B). Both genotypes received rewards on more than 90% of trials on average, although the WT mice had significantly more trials with no rewards, likely due to the differences in lick rates (Figures 1D, S1D, S1F, and S1G). To confirm that animals were using visual cues to perform the spatial task, we assessed these same behavioral metrics in a circular track with no visual cues after training in the task with visual cues, and we found that miss rate and lick latency until reward significantly increased in the track without cues (Figures 1E–1G, S1C, and S1E). We thus demonstrated that both *5XFAD* and WT mice licked for reward in a specific location using visual cues in a VR spatial task.

Interneuron-to-pyramidal (INT-to-PYR) monosynaptic connections are weaker in 5XFAD mice

Using this task, we then examined how synapses and neural activity differ between *5XFAD* mice and WT littermates. We first focused on whether synaptic efficacy was altered *in vivo* in *5XFAD* mice. We recorded local field potential (LFP) and single-unit activity of 2,447 neurons (*5XFAD*, 170.38 ± 15.36 single units per animal over multiple sessions, $n = 8$; WT, 180.67 ± 17.12 single units per animal, $n = 6$) in hippocampal CA1 of *5XFAD* and WT animals (11–14 months) performing the spatial task interleaved with no task periods (see STAR Methods, Figure S2, and Table 1). We assessed neural activity in hippocampal CA1 since it is a major output region of the hippocampal circuit, which is affected early in AD (Braak and Braak, 1991). To assess synaptic connections in awake behaving animals, we used a well-established method of measuring synaptic connectivity and connection strength from extracellular recordings (Alonso et al., 1996; Barthó et al., 2004; English et al., 2017; Fujisawa et al., 2008; Perkel et al., 1967; Reid and Alonso, 1995; Tanaka, 1983; Toyama et al., 1981; Usrey et al., 1999). In this method, putative monosynaptically connected cell pairs are identified by computing spike train cross-correlations and finding pairs of cells with significant increases or decreases in cross-correlations at time lags consistent with monosynaptic connections, that is, 1–3 ms (see STAR Methods). Putative excitatory and

inhibitory connections were identified by detecting significant peaks or troughs at a 1- to 3-ms lag in the cross-correlogram (CCG) compared to the pairs' shuffled CCGs (spike trains jittered on a ± 5 -ms time scale; Diba et al., 2014; Fujisawa et al., 2008; Figures 2A, 2B, and S5). This method preserves the longer time scale temporal dynamics of neural spike trains and thus has the advantage of identifying pairs that have spiking co-occurrences on time scales that cannot be explained by broader firing rate changes. This analysis was performed across all cells recorded in CA1, producing an effectively random sampling of putative monosynaptically connected pairs.

We then determined whether these monosynaptic connections differed between *5XFAD* and WT mice by quantifying their connection strength or functional synaptic efficacy (Figures 2A and 2B; see STAR Methods). We measured synaptic efficacy during periods with theta oscillations (when animals are running), SWRs, and non-theta periods (when animals are quiescent and SWRs occur) to determine whether differences between *5XFAD* and WT mice occurred during specific network states. Interestingly, we found that the inhibitory connection strengths of interneurons onto pyramidal cells, that is, the magnitude of the inhibitory troughs, were lower in the *5XFAD* mice compared to their WT littermates. This inhibitory connection strength was observed to be 63.16% smaller during SWR periods in *5XFAD* mice (Figure 2C, 2D, and S3A), 43.77% smaller during non-theta periods (Figures 2E, 2F, and S3B), and 38.38% smaller in *5XFAD* mice during theta periods (Figures 2G, 2H, and S3C). Importantly, these changes in connection strength could not be explained by differences in firing rate between genotypes (Figure 2I). For INT-to-PYR cell pairs, there were no significant differences in firing rate (Figure 2I). Furthermore, our cross-correlation normalization method controlled for firing rate differences for the specific time periods used in the connection strength analysis (see STAR Methods). We controlled for differences in SWR duration and spike numbers between *5XFAD* and WT groups and found the WT mice still had larger inhibitory trough magnitudes than did the *5XFAD* mice using multiple subsampling approaches (see STAR Methods and Figures S3E and S3F).

In contrast to the INT-to-PYR connections, the connection strength of pyramidal-to-interneuron (PYR-to-INT) connections did not differ significantly between *5XFAD* and WT mice. PYR-to-INT connections were weaker in the *5XFAD* mice compared to WT mice, most noticeably 48.57% weaker during SWR events and 34.91% weaker during theta periods (Figures 3A, 3B, 3E, 3F, S4A, and S4C). These trends were less clear during non-theta periods (Figures 3C, 3D, and S4B). For PYR-to-INT cell pairs, there were also no significant differences in firing rate (Figure 3G). We also found similar results using multiple subsampling approaches to control for differences in spike numbers between *5XFAD* and WT groups during SWRs (see STAR Methods and Figures S4E and S4F). In summary, these results demonstrate that *5XFAD* mice exhibit significantly weaker INT-to-PYR connection strengths that were dependent on the network state during awake behavior, with the most prominent synaptic deficits occurring during SWRs.

We then asked whether the proportions of monosynaptically connected cells were altered in these mice compared to WT littermates. We found that the proportion of INT-to-PYR connections were greater in WT mice, while the proportion of detectable PYR-to-INT connections were not significantly different between *5XFAD* and WT mice (Figures S3D

and S4D). Overall, the proportions of cells with detected connections between pyramidal cells and interneurons were similar to previous monosynaptic connection analyses in WT rats (Fujisawa et al., 2008). These differences in the proportion of connected cells were not due to the location of those cells within the pyramidal layer (Figure S5). These results show that *5XFAD* mice have a smaller proportion of detectable INT-to-PYR connections.

5XFAD mice have shorter and fewer SWRs compared to WT mice

Interactions between interneurons and pyramidal cells are essential to SWR generation and maintenance (Alger and Nicoll, 1982; Buzsáki, 1986; Buzsáki et al., 1983; Csicsvari et al., 1999; Klausberger et al., 2003; Pouille and Scanziani, 2001; Stark et al., 2014; Ylinen et al., 1995), and previous work has shown decreased abundance of SWR events in *5XFAD* mice at a younger age (3–4 months old, Iaccarino et al., 2016). Since we observed deficits in interneuron and pyramidal cell monosynaptic connections, we wondered whether SWRs were also disrupted in these older *5XFAD* mice. We found that there was an 82.43% decrease in SWR abundance on average in *5XFAD* versus WT mice (Figures 4A, 4B, and S6A). The *5XFAD* mice also had 27.27% more periods with no SWR events (Figure 4C). These differences in SWR abundance were not an effect of variations in non-theta periods (see STAR Methods and Figures S6B and S6E). We then examined the characteristics of the remaining SWRs in the *5XFAD* mice. While the average LFP traces looked relatively typical in *5XFAD* and WT mice, showing that the hallmark features of ripples are intact (Figure 4D), when we quantified duration and power of the remaining ripples, we found significant but small decreases in the *5XFAD* mice. The SWRs that remained in the *5XFAD* mice were 18.18% shorter in duration on average and had 10.88% decreased amplitude on average (Figures 4E, 4F, S6C, and S6D). These results indicate a large deficit in the generation and maintenance of SWR events in *5XFAD* mice.

Place cells of 5XFAD mice have decreased reactivation during SWRs

In light of altered synaptic connections and SWRs in CA1, we asked whether *5XFAD* mice have altered hippocampal neural codes, such as the encoding of spatial information via place cells or the activation and reactivation of place cells during SWRs, both of which are important for cognitive processes such as spatial memory (Davidson et al., 2009; Diba and Buzsáki, 2007; Foster and Wilson, 2006; Karlsson and Frank, 2009; O'Neill et al., 2008; Stella et al., 2019; Wilson and McNaughton, 1994). Both *5XFAD* and WT animals had pyramidal cells with spatially tuned firing, e.g., place cells (Figure 5A; see STAR Methods). Interestingly, several place cells had multiple peaks that seemed to follow the repetitive visual cues and reward zones present on the VR track (Geiller et al., 2017; Figure 5A). We found that place cells in the *5XFAD* mice had 12.5% less spatial information content on average (Figures 5B and S7A) and 13.88% lower peak firing rates, but neither were significantly different (Figures 5C and S7B).

We then determined whether *5XFAD* mice had lower place cell reactivation during SWRs. Because there were far fewer SWR events in *5XFAD* mice and the remaining SWRs were shorter in duration, we measured reactivation of place cell pairs during SWRs to include as many SWRs as possible. If coherent sequences of neural activity are reactivated during SWRs, two cells that fire closely together during theta will also fire closely together during

SWRs. Thus, to assess reactivation among cell pairs, we first identified place cell pairs that fire closely together during theta (within ± 35 ms) and then asked how closely those same cells fired together during SWRs. In WT mice place cell pairs firing near in time during theta fired on average 27.46% more closely together during SWRs than did *5XFAD* mice (Figures 5D, 5E, and S7C). We still found weaker reactivation in *5XFAD* than in WT mice when we controlled for differences in spike numbers between *5XFAD* and WT groups (see STAR Methods and Figures S7G and S7H). We also analyzed SWR activation in terms of coactivation probability of cell pairs and found that the coactivation probability of place cells during SWRs was 78.18% lower in *5XFAD* mice than in WT mice on average (Figures 5F and S7D). Activation probability of place cells was also lower in *5XFAD* mice (Figures 5G and S7E). We found that pyramidal cell and interneuron z-scored peak firing activity did not significantly differ during SWRs in the *5XFAD* mice (Figure S7F). There were small differences in the location of recorded cells in the layer between genotypes, but the differences were on average 12 μm for pyramidal cells and 33 μm for interneurons, which are close to our resolution for measuring distance between channels (27.5 μm , Figure S2). These results demonstrate that *5XFAD* mice have relatively intact spatial information content while they have much lower coactivation and coordinated reactivation of those place cells during SWR events. Thus, *5XFAD* mice have compounding deficits; they have drastically fewer and shorter SWRs, as well as less place cell activation and reactivation during the few remaining SWR events.

DISCUSSION

In this study, we used *in vivo* electrophysiological recordings of many single neurons in hippocampal CA1 to identify synaptic connection and neural coding deficits in the *5XFAD* mouse model of AD. We discovered that *5XFAD* mice had significantly weaker inhibitory synaptic efficacy onto pyramidal cells in awake animals during SWRs compared to WT mice. Because interneuron and pyramidal cell activities are critical for SWR oscillations, we then examined SWR activity. We found that *5XFAD* mice had 82% fewer SWRs on average, as well as 18% shorter SWRs on average. Finally, while spatial information of place cells was relatively intact in *5XFAD* mice, we found significant impairments in activation, coactivation, and coordinated reactivation of these cells during SWRs. These results demonstrate synaptic dysfunction, shorter SWRs, and weaker place cell reactivation during SWRs in an awake, behaving mouse model of AD.

Linking synaptic dysfunction and interneuron deficit hypotheses in AD

Synaptic dysfunction in AD has been of special interest because synaptic loss is one of the best correlates of cognitive impairment in AD (DeKosky and Scheff, 1990; Terry et al., 1991). Prior work has found that spatial memory impairment in *5XFAD* mice is correlated with molecular markers of synaptic degeneration, measured via decreased levels of pre-synaptic (syntaxin, synaptophysin) and post-synaptic (PSD-95) markers (Oakley et al., 2006; Schneider et al., 2014; Xiao et al., 2015). Furthermore, synaptic function has important implications outside of learning and memory deficits; synaptic dysfunction plays a key role in a wide variety of neurodevelopmental and neurodegenerative diseases, and inhibitory synapses are critical to maintain synchronized network oscillations such as SWRs (Bartos et

al., 2002, 2007; Coghlan et al., 2012; Gonzalez-Burgos and Lewis, 2008; Isaacson and Scanziani, 2011; van Spronsen and Hoogenraad, 2010; Stephan et al., 2006). Prior research examining spine density of pyramidal cells in *5XFAD* mice found significant spine loss in somatosensory cortex, prefrontal cortex, and hippocampus (Crowe and Ellis-Davies, 2014; de Pins et al., 2019). Another study investigating synaptic activity in *5XFAD* mice *in vitro* found an increase in the ratio of excitatory-to-inhibitory charge in pyramidal cells and a decrease in this ratio in parvalbumin (PV)⁺ interneurons; however, they observed increased SWR frequency and amplitude, contrary to our findings in awake, behaving animals (Caccavano et al., 2020). While there has been extensive previous work on the role of amyloid beta on synaptic activity *in vitro* (Abramov et al., 2009; Petrache et al., 2019; Puzzo et al., 2008) or in anesthetized animals *in vivo* (Chapman et al., 1999; Freir et al., 2001; Stéphan et al., 2001), no prior studies have investigated these synaptic changes in awake, behaving animals. Thus, it was not clear exactly how previously characterized synaptic changes would affect synaptic efficacy in awake animals.

Recent studies have also revealed inhibitory interneuron dysfunction in AD mice. Several studies have shown the loss of PV₊ inhibitory interneurons in *5XFAD* mice (Ali et al., 2019; Flanigan et al., 2014; Giesers and Wirths, 2020). Both *hAPP* mice and human patients with AD have lower levels of sodium channel Nav1.1 specifically in inhibitory interneurons. In *hAPP* mice, which overexpress amyloid precursor protein (APP) due to two human familial AD mutations (Games et al., 1995), implanting interneurons that overexpressed Nav1.1 sodium channels rescued gamma activity deficits and epileptic-like network hypersynchrony previously observed in these mice, as well as improved cognitive function (Martinez-Losa et al., 2018; Palop et al., 2007; Verret et al., 2012). In *apoE4* mice, which express the major genetic risk factor for late-onset sporadic AD, GABAergic dysfunction and interneuron loss in the dentate gyrus is correlated with deficits in learning and memory (Leung et al., 2012; Li et al., 2009). In *APP23xPS45* mice, a model that overexpresses both APP and mutant presenilin, hyperactivity was reduced by increasing inhibition with a GABA-a receptor channel agonist (Busche et al., 2008). Thus, there is evidence for deficits in inhibitory activity in multiple brain regions and mouse models of AD. Of course, no mouse model recapitulates AD faithfully (Scearce-Levie et al., 2020). For example, the *5XFAD* mouse model used in this study does not mimic all of the symptoms of human AD, most notably they lack neurofibrillary tangles, a major hallmark of AD (Oakley et al., 2006). Furthermore, the *5XFAD* mouse model is a relatively aggressive model with a rapid progression. However, converging evidence from multiple mouse models with different genetic pathogenesis suggests that inhibitory interneurons are especially vulnerable.

Our findings connect these two lines of research by showing a deficit in inhibition on the synaptic level. We found deficits in interneuron inhibition onto pyramidal cells in a mouse model of AD. While spine loss and inhibitory deficits have been previously characterized in AD models *in vitro* or in post-mortem tissue, our work reveals how these deficits manifest in awake behaving animals. Importantly, note that measuring synaptic connectivity *in vivo* is a complicated task, and the main limitation of our results is that cross-correlation measures only indirectly infer monosynaptic connectivity and connection strength. Additionally, the overall number of detected connections is lower than is thought to be physiologically present. This approach is limited in that it does not detect all synaptic connections; for

instance, it cannot accurately detect connections in cells with low firing rates, and it quantifies spike transmission but not postsynaptic potentials. Even considering these limitations, this method of detecting monosynaptic connections and measuring synaptic strength is well established, has been used in many other studies, and has been validated with optogenetic and juxtacellular stimulation (Alonso et al., 1996; Barthó et al., 2004; Reid and Alonso, 1995; English et al., 2017; Fujisawa et al., 2008; Perkel et al., 1967; Tanaka, 1983; Toyama et al., 1981; Usrey et al., 1999; Vizuete et al., 2012). In short, our findings reveal deficits in inhibitory synaptic strength during behavior, linking prior work on synaptic dysfunction and interneuron deficits.

Synaptic changes and SWR deficits could underlie memory impairment

The observed deficits in interneuron connection strength onto pyramidal cells could explain the decreased abundance, power, and duration of SWRs in *5XFAD* mice. Importantly, SWRs are present and associated with memory in both rodents and humans (Axmacher et al., 2008; Buzsáki, 2015; Carr et al., 2011; Girardeau and Zugaro, 2011; Girardeau et al., 2009; Jadhav et al., 2012; Pfeiffer and Foster, 2013; Singer et al., 2013; Staresina et al., 2015; Vaz et al., 2019). Prior work shows that both interneuron and pyramidal cell activity is critical for SWR oscillations (Buzsáki, 2015; Schlingloff et al., 2014; Stark et al., 2014). Furthermore, inhibition is thought to prolong the recruitment of excitatory pyramidal cells during SWRs (Csicsvari et al., 1999; Klausberger et al., 2003), and optogenetic stimulation of inhibitory cells can initiate SWR events (Schlingloff et al., 2014). Pharmacologically disrupting GABA receptor activity results in fewer and shorter ripples, similar to our findings in *5XFAD* mice (Ponomarenko et al., 2004). Intriguingly, we observed more pronounced inhibitory deficits during SWRs. Fewer and shorter SWRs could underlie cognitive deficits in these mice because SWRs are essential for intact memory consolidation. Indeed, longer SWRs are associated with improved memory performance, and SWR abundance predicts spatial memory impairments (Fernández-Ruiz et al., 2019; Jones et al., 2019). SWR deficits have also been observed in multiple mouse models of AD (Gillespie et al., 2016; Iaccarino et al., 2016). This converging evidence from multiple animal models of AD suggests the intriguing possibility that multiple molecular pathologies underlying AD could produce similar deficits in SWRs.

During SWRs, ensembles of hippocampal place cells that were previously active during exploration are reactivated in an experience-dependent manner (Davidson et al., 2009; Diba and Buzsáki, 2007; Foster and Wilson, 2006; Karlsson and Frank, 2009; O'Neill et al., 2008; Stella et al., 2019; Wilson and McNaughton, 1994). Disruption of SWR events is thought to impair memory and results in worse behavioral performance on a spatial navigation memory task (Girardeau et al., 2009; Jadhav et al., 2012). Furthermore, higher reactivation, as measured by coactivation of place cells during SWRs, predicted a higher likelihood of the animal performing correctly on the next trial in a spatial memory task (Singer et al., 2013). Interestingly, we found decreased coactivation of place cell pairs and weaker reactivation during SWRs. Although we did not observe task performance impairments due to the simplicity of our task, several prior studies of *5XFAD* mice have found spatial and memory impairments (novel object location, novel object recognition, Morris water maze) at or before this age (Flanigan et al., 2014; Martorell et al., 2019; O'Leary et al., 2018; Oakley et

al., 2006; Xiao et al., 2015). Taken together, these findings of disrupted place cell activation and reactivation during SWRs could be a mechanism of spatial memory impairment observed in mouse models and humans with AD.

Our findings reveal inhibitory synaptic changes, shorter SWRs, and disrupted place cell reactivation during SWRs in an awake mouse model of AD during behavior. In line with previous work, these results point to an important role for both synaptic dysfunction and inhibition deficits in AD (Palop and Mucke, 2016; Selkoe, 2002). Based on the role of inhibition in SWR generation and maintenance and the fact that SWRs are essential for spatial memory in healthy mice, these findings suggest a mechanism by which synaptic deficits in AD lead to dysfunction of neural activity and neural codes essential for memory.

STAR★METHODS

RESOURCE AVAILABILITY

Lead contact—Further information and requests for resources and reagents should be directed to the Lead Contact, Annabelle C. Singer (asinger@gatech.edu).

Materials availability—This study did not generate new unique reagents.

Data and code availability—Data and code available upon reasonable request.

EXPERIMENTAL MODEL AND SUBJECT DETAILS

Animals—All animal work was approved by the National Institute of Health guidelines on animal care and use at Georgia Institute of Technology. Male (11-14 month-old) *5XFAD* and *WT* mice on a C57BL/6 background were either obtained from the Jackson laboratory (F1, F7, F8) or bred in the animal facilities at Georgia Institute of Technology. All mice were littermates (Table 1). Mice were single-housed on a reverse 12-hour light/12-hour dark cycle, and all electrophysiology and behavioral experiments were performed during the dark cycle. At the start of the behavioral and electrophysiological experiments, mice were food-restricted between 85%–90% percent of their baseline body weight, and water was provided without restriction. Animals were excluded from further behavioral training and electrophysiological recording if they developed any health problems (2 animals) or if they never licked in response to reward during behavioral training (1 animal). The experimenter was blind to genotype during behavior, recording, and preprocessing analysis of data.

METHOD DETAILS

Surgical procedures—Mice were anesthetized with isoflurane before headplate implant surgery. A custom stainless steel headplate was fixed to the skull using dental cement (C&B Metabond, Parkell), and the target craniotomy site for LFP recordings was marked on the skull (in mm, from bregma: –2.0 anterior/ posterior, +/-1.8 medial/lateral for CA1). Craniotomies were later performed in 11-14 month-old mice before electrophysiology recording sessions. These craniotomies (200-500um diameter) were made by using a dental drill to thin the skull and then opening up a small hole in the skull with a 27-gauge needle.

Craniotomies were sealed with a sterile silicone elastomer (Kwik-Sil WPI) and only opened for recording experiments.

Behavioral training and analysis—The virtual reality annular track environment was designed using ViRME_n (Aronov and Tank, 2014) open-source software and displayed on a cylindrical screen using an HD projector system reflected by several mirrors. To begin the behavioral task, head-fixed animals ran on a spherical treadmill composed of an 8-inch polystyrene foam ball floating on air. Animals either immediately began behavioral training in the virtual reality environment the first time they were head-fixed on the treadmill ($n = 11$), while others were given 1-3 days of habituation to the treadmill without the virtual reality projector system turned on ($n = 3$). The transition to habituation without VR occurred because we observed animals became more comfortable more quickly with the VR turned on. Animals ran on the ball and their translational and rotational velocities were tracked via an optical mouse and converted into movement through the virtual reality environment. In the first phase of behavioral training, animals navigated around the annular track environment and received a sweetened condensed milk reward (1:2 water dilution) when they entered either of the two patterned reward zones. These locations were indicated with visual cues, and the reward location was the second instance of a patterned visual cue on each lap around the circular track. An average trial was approximately 9 m around the entire annulus, however the exact distance traveled varied from trial to trial. Once animals began demonstrating anticipatory licking before the reward zone, the animals were transitioned to the second phase of the behavioral task. In the second phase of behavioral training, animals navigated around the annular track and licked in the reward zone in order to receive a reward (Figure S1). The second phase of behavioral training was the same environment and used the same visual cues as the first phase of training. Licks were detected using a photo-interrupter placed in front of the animal's mouth around the reward spout. In one group of animals ($n = 5$), electrophysiology recordings began when the animal successfully transitioned from the automatic reward delivery phase to the second phase of the task. In another group of animals ($n = 5$), electrophysiology recordings began after the animals demonstrated more than 2 days of licking for reward behavior (see Behavioral analysis below). All of the behavioral analysis was performed on data from the second phase of the behavioral tasks during which the animals had to lick to receive the reward.

Raw behavioral data tracking translational and rotational velocity, licks, position, and time were analyzed using MATLAB®. Position and velocity data were smoothed using a moving average and all data was segmented into trials in which each trial was one full lap (360 degrees) around the annular track in which the animal passed through two reward zones. Data were then combined across behavioral sessions into trial blocks of 50 trials each. We quantified lick latency as the number of degrees from entering the reward zone until the animal received its first reward. We quantified miss rate, with a miss consisting of a trial where the animal received no reward in either of the two reward zones. We also quantified lick and velocity rate as licks per second and degrees traveled in the track per second respectively. Finally, for comparisons between the track with and without visual cues, we analyzed data from the last two sessions in the track with cues and the first two sessions of the track without visual cues.

Electrophysiology recordings—All recordings were performed using the same virtual reality and treadmill set-up as described above. Animals were head-fixed on the treadmill for a maximum five-hour-long recording session, with one recording session per day (number of sessions ranged from 1-4 per animal, Table 1, Figure S1). A 32-channel, single shank probe (NeuroNexus) was placed in a slightly different location within the craniotomy at the beginning of each recording session and advanced vertically to the CA1 pyramidal layer of hippocampus identified via electrophysiological characteristics: large theta waves, sharp-wave ripples, and 150+ μ V spikes on multiple channels. Recording sites (250 μ m from farthest sites) spanned the layer (Figure S3). Recordings consisted of interleaved periods of behavioral task performance when animals navigated through the virtual reality environment, and no-task periods, during which no virtual reality environment was displayed on the screen (Figure S1). Though we did not explicitly quantify sleep during the task, we observed that animals head-fixed on the spherical treadmill were either moving or maintaining their balance on the ball and thus were very unlikely to be sleeping during these recordings. We also observed that most non-theta periods (when the animals are still) were less than 30 s long on average, and therefore unlikely to include sleep. Data were acquired with a sampling rate of 20 kHz using an Intan RHD2000 Evaluation System using a ground pellet as reference.

LFP analyses—LFP was obtained by downsampling raw traces to 2kHz and bandpass filtering between 1-300Hz. Outliers were eliminated by interpolating over outliers when the pre-filtered LFP signal were 7 standard deviations above the mean. All LFP analyses used the signal from a single channel that was putatively located in the stratum pyramidale. To identify this channel, the LFP was bandpass filtered for the sharp-wave ripple band (150-250 Hz, see details below) and the average of the sharp-wave ripple band envelope over time was calculated from each channel. The channel with the highest average sharp-wave ripple band power was used for all further analyses, and this channel was predominately located in the middle of the depth-wise span of the NeuroNexus probe. In order to ensure that probe depth placements were similar across genotypes, we analyzed the distribution of ripple power across all channels for all recording sessions, centered by the LFP channel.

LFP was used to detect theta, non-theta, and sharp-wave ripple periods. To detect theta periods, the LFP was bandpass filtered for theta (4-12 Hz), delta (1-4 Hz), and beta (12-30 Hz) using an FIR (finite impulse response) equiripple filter. The envelope amplitude of the filtered theta signal was divided by the sum of the envelope amplitudes of the delta and beta signals. A theta period was defined as a period during which this theta to delta and beta ratio was 2 standard deviations above the mean for at least 2 s (Csicsvari et al., 1999; Iaccarino et al., 2016; Jackson et al., 2006). Theta periods were visually inspected to ensure that the criteria used accurately included theta periods. To detect non-theta period, the same theta to delta and beta ratio as described above was used. A non-theta period was defined as a period during which this ratio threshold was less than 1.1 for at least 2 s. Non-theta periods were visually inspected to ensure that the criteria used accurately included non-theta periods. To detect sharp-wave ripple events, the LFP was bandpass filtered for the sharp-wave ripple band (150-250 Hz) using an FIR equiripple filter. Sharp-wave ripples were detected when the envelope amplitude of the filtered sharp-wave ripple trace was greater than 3 standard

deviations above the mean for at least 20 ms (Karlsson and Frank, 2009; Singer and Frank, 2009; Singer et al., 2013). We excluded any events that had an LFP amplitude greater than 1500 μV or less than $-1500 \mu\text{V}$ to eliminate artifacts. We also applied a power ratio threshold (power from 100 to 250 Hz / power from 250 to 400 Hz) based on the typically observed frequency range of sharp-wave ripples (Ylinen et al., 1995). We excluded any detected events that had a power ratio less than 4. Sharp-wave ripples were visually inspected to ensure that the criteria used accurately detected sharp-wave ripple events.

Duration of sharp-wave ripples was defined as the length of time the sharp-wave ripple envelope was greater than the threshold of 3 standard deviations above the mean. Gamma power before, during, and after SWRs was computed by filtering the LFP for low gamma and z-scoring the amplitude of the envelope of the Hilbert transform. Sharp-wave ripple power was quantified as standard deviations above the mean ripple power for the entire recording session.

Classification of cell types—Spike detection and sorting were performed using MountainSort automated spike sorting and automated curation, followed by manual curation guided by visual inspection of waveforms and cross-correlograms (Chung et al., 2017). Prior to manual curation, automatic curation was performed by applying quality thresholds to include units with a peak signal to noise ratio (SNR) greater than or equal to 1, less than 10% overlap with noise, and greater than 95% isolation against other units. To account for periods of instability in the recordings during which single units were lost, stability criteria were applied such that only stable periods (no sudden loss of a single unit's firing rate) would be considered in analysis. Firing rate (FR) for each unit was computed throughout the recording session. Firing rate was clustered into two distributions, low FR and high FR, using k-means clustering. A stable period was defined as the longest length of time that the FR was 2 standard deviations above the low FR mean. If the firing rate of the unit never dropped below 10% of the high FR mean, the stable period was defined as the whole recording session.

Cell types were classified into putative pyramidal cells and putative interneurons based on the spike width and the first moment of the autocorrelogram. These measurements are well-established metrics used for cell-type classification (Barthó et al., 2004; Csicsvari et al., 1998, 1999; Niell and Stryker, 2008; Senzai et al., 2019). Spike width was calculated as the length in milliseconds from the negative peak of the spike to the positive trough, where the trough was defined as the first instance when the differential of the waveform was equal to 0. The first moment of the autocorrelogram was calculated as the center of mass along the time-axis of an autocorrelogram calculated with lags of 0 to 50 ms. Single units were excluded if the autocorrelograms had a peak spike count less than 10. Mean firing rate was computed for each single unit and only stable periods for each unit contributed to the mean FR calculation (described above). The three parameters (spike width, firing rate, autocorrelogram moment) were then plotted for all single units, and these plots revealed two clear clusters that could be isolated using the spike width and autocorrelogram moment parameters. Putative pyramidal cells were defined as units that had a spike width greater than 0.5 ms and a first moment of the autocorrelogram less than 5 ms. Putative interneurons were defined as units that had a spike width less than 0.5 ms and a first moment of the

autocorrelogram greater than 4 ms. Overall these thresholds for spike width and first moment of the autocorrelogram are similar to previously reported classification criteria, although the autocorrelogram function is dependent on the window it is measured within (Csicsvari et al., 1998, 1999; Senzai et al., 2019). This classification was further validated by the identification of putative monosynaptic connections (described below). Only units localized in the two predominant clusters were included in further analyses, and as a result, several neurons were unclassified and excluded. In order to ensure we were not sampling from different populations of interneurons and pyramidal cells across genotypes (i.e., superficial or deep neurons relative to CA1), we inspected the population of classified interneurons and pyramidal cells for all recording sessions, centered by the LFP channel (the channel with the highest ripple power).

Identification of monosynaptic connections—Analysis for the identification of putative monosynaptic connections was drawn from previous studies (Amarasingham et al., 2012; Fujisawa et al., 2008; Hatsopoulos et al., 2003). To identify connections, cross-correlations were calculated between spike trains of all cell pairs with lags from 0 to 50 ms. Out of all detected cells, there were 110,132 possible connections in *5XFAD* mice and 87,320 in *WT* mice (counting each actual pair of cells twice for both directions of connectivity). If the spike train cross-correlation pair had no bins with a spike count of less than 2.5, then a jittered cross-correlation was calculated 200 times for all cell pairs. Spike trains of the second neuron were jittered such that each spike time was shifted by a random integer value between -5 and $+5$ ms. This approach preserved the longer timescale temporal dynamics of the spike trains while removing any spiking correlations not due to monosynaptic connections. The maximum and minimum of the 200 shuffled cross-correlations were then taken and defined as the significance bands. If the original cross-correlation between the cell pair was greater than the significance band maximum at lags of 1-3 ms, then the pair was classified as an excitatory monosynaptic connection. If the cross-correlation between the cell pair was less than the significance band minimum at lags of 1-3 ms, then the pair was classified as an inhibitory monosynaptic connection. We were careful to only include single unit pairs with good isolation, so all pairs that shared the same principal channel, or recording channel on which the amplitude of the spike was largest, were discarded from further analyses. We also separated cell types based on spike width and firing properties. Furthermore, all cross-correlograms were manually curated by inspecting the cross-correlograms and waveforms across all recording channels (Figure S5). Pairs were excluded if the waveforms looked similar and the cross-correlograms appeared to be autocorrelograms (a very large peak or trough at 0 ms). Furthermore, the excitatory (peak) or inhibitory (trough) properties of the connected units were further confirmation of their cell type classification. In order to ensure there were no differences in the sampling of monosynaptically-connected cell pairs across the depth of the probe, we also inspected the distribution of putatively connected cell pairs across the recording probe, centered using the channel with the peak ripple power (Figures S8 and S9). We also observed that several of the detected interneuron-to-pyramidal (INT-to-PYR) connections were likely reciprocally driven by pyramidal cells, as evidenced by the large excitatory peak in the -3 to -1 ms range (Figures 2C, 2E, and 2G). Notably, we detected interneuron to pyramidal connections solely based on the presence of a significant inhibitory trough in the 1-3 ms range.

Quantification of connection strength—To quantify connection strength of excitatory and inhibitory pairs, cross-correlograms were calculated for all putative monosynaptically connected pairs (see Identification of putative monosynaptic connections) during different periods, such as when theta was detected (see LFP analyses). These cross-correlograms were then normalized by the geometric mean firing rate to control for any possible firing rate differences between pairs. These firing rates were calculated for the subset of time windows during which connection strength were analyzed. To control for differences in sharp-wave ripple duration between genotypes, we also used the same time window around the midpoint of the sharp-wave ripple for all analyses of connection strength during sharp-wave ripples. To calculate the connection strength, we took the peak or trough of the normalized cross-correlograms over 1-4 ms time lags, and subtracted the average of the normalized baseline cross-correlogram, specifically the baseline at lags from 5 to 6 ms or 1 ms beyond the monosynaptic connection latency windows. Thus, this peak magnitude value was a metric of the increase or decrease in spiking activity due to the monosynaptic connection, while controlling for baseline firing activity. Since these cell pairs had previously been identified as putative excitatory or inhibitory connections based on the cross-correlations over all time, we rectified any opposite-signed values (e.g., an excitatory connection with a negative peak value, less than 7% of all cases) to zero to correct for pairs that likely did not fire enough spikes or were too noisy during the periods we analyzed. We also performed the same analysis but removed all opposite-signed values from the analysis entirely and found similar results. For plotting purposes, all cross-correlogram averages are displayed as a difference from baseline.

To control for the potential that differences in spike numbers between *5XFAD* and *WT* groups during sharp-wave ripples contributed to the observed differences in trough and peak magnitudes, we subsampled spikes in the *WT* group so that both *5XFAD* and *WT* groups had a similar number of spikes total. We matched total spike counts during sharp-wave ripples between *5XFAD* and *WT* groups using two approaches. In both approaches, both groups had approximately the same number of spikes total after subsampling, erring on the side of the *5XFAD* group having more spikes if the numbers were not exactly the same. In one approach, spikes were removed from spike trains of the *WT* cells before calculating the cross-correlograms and the monosynaptic connection strengths. First, we matched each *5XFAD* recording session with a *WT* session with the smallest difference in spike counts between them without replacement. Spikes were then randomly selected for removal from the *WT* cell pairs so that the corresponding *WT* session had the same or fewer spikes as the matched *5XFAD* session. Connection strengths were then computed. This spike removal subsampling process and connection strength calculation was repeated 50 times and then averaged across the 50 subsampling events so that each *WT* pair had one metric of connection strength. To ensure a reasonable number of spikes were included in the measurement of connection strength, we also only included pairs with at least 200 spikes across all sharp-wave ripple periods. We found similar results using another approach in which we used the original spike trains but then removed cell pairs from the *WT* group in order to match the spike count total of the *5XFAD* group. Across both of these subsampling analyses, we found similar trends as the full dataset. Furthermore, we found no evidence that

differences in synaptic strength were due to differences in firing rates of the neurons or in the cells' spatial position in the CA1 layer.

Place cell identification—To quantify place cells, we calculated an occupancy-normalized firing rate map of putative pyramidal cells as a function of position on the annular track, using spike counts and time spent in 2-degree bins each smoothed with a Gaussian curve. Two degrees is equivalent to 1/180th of the track, which is approximately equivalent to 5 cm physical distance on the ball. These firing rate maps were calculated only using the cell's stable times (as described above). Spatial information for pyramidal cells was then calculated using the firing rate maps by applying the following equation:

$$Spatial\ information = \sum_i p_i \frac{\lambda_i}{\lambda} \log_2 \frac{\lambda_i}{\lambda}$$

Where p_i was the probability the animal was in the i th bin, λ was the mean firing rate of the cell, and λ_i was the firing rate of the cell in the i th bin (Langston et al., 2010; Skaggs et al., 1996). We then defined a place cell as any pyramidal cell with a peak firing rate greater than 1 Hz, an average firing rate of less than 10 Hz (to exclude potential interneurons), and a spatial information content in the 95th percentile or above compared to the shuffled spike train data. Because these place cells were recorded in mice and in virtual reality, which tend to have lower spatial information, spatial information is expected to be lower than rats and than recordings made in the real world (Ravassard et al., 2013).

Reactivation during sharp-wave ripples—We examined place cell pair reactivation, activation probability, and pairwise coactivation probability during sharp-wave ripples to assess sharp-wave ripple reactivation while including as many sharp-wave ripple events as possible since *5XFAD* mice had significantly fewer sharp-wave ripples. Standard replay analyses criteria, such as a minimum number of cells active per sharp-wave ripple event, would have biased our analyses against the typical sharp-wave ripples found in the *5XFAD* mice (ripples with shorter duration and altered pyramidal cell firing activity). Instead, we used measures of coactivation and reactivation that assess coordinated spike timing of pairs of cells. Coactivation probability during SWRs in particular is predictive of behavioral performance (Singer et al., 2013). Coactivation probability was calculated by first identifying how many sharp-wave ripples occurred in which a pair of place cells was both stable and active, and then dividing this number by how many total sharp-wave ripples occurred in which the same pair of cells was stable (see Spike sorting and single unit stability). Activation probability was calculated similarly, but for single cells instead of pairs of cells. Notably, this analysis is different from analyzing firing activity during sharp-wave ripple events, because we specifically test the activation of place cells and place cell pairs (not all cells), and this metric tests the proportion of sharp-wave ripple events in which place cells are active, not the average firing rate of all cells during sharp-wave ripple events. To assess place field similarity and reactivation during sharp-wave ripples, we examined relative spike timing of place cell pairs during theta and compared it to relative spike timing during sharp-wave ripples. We quantified spiking near in time versus far in time by taking the sum of the place cell pair cross-correlogram during theta at short time lags (−35ms to +35ms) versus

the sum of the cross correlogram during theta at longer time lags (-70 to -35 ms, and $+35$ to $+70$ ms). We converted this to an activity index (short time lag activity – long time lag activity / short time lag activity + long time lag activity), in which a place cell pair with the majority of its spiking within a 70ms window would have a value of 1. We used this activity during theta index to sort these place cell pairs, and examined the cross-correlograms of the same place cell pairs during sharp-wave ripples. We then quantified relative spike timing during sharp-wave ripples as the absolute value of the lag of the maximum correlation value. For these analyses, we excluded sessions with less than 10 sharp-wave ripples because reactivation measures are less accurate over fewer ripples. We found similar results if we included all sessions. To control for the potential that differences in spike numbers between *5XFAD* and *WT* groups during sharp-wave ripples contributed to the observed differences in relative spike timing during sharp-wave ripples, we subsampled spikes in the *WT* group so that both *5XFAD* and *WT* groups had a similar number of spikes total. We matched total spike counts between *5XFAD* and *WT* groups using multiple approaches. In one approach, spikes were removed from spike trains of the *5XFAD* and *WT* cells before calculating the relative spike timing during sharp-wave ripples. First, we matched each *5XFAD* recording session with a *WT* session with the smallest difference in spike counts between them without replacement. Spikes were randomly selected for removal from the *WT* cell pairs if the *WT* session had more spikes than the corresponding *5XFAD* session. Relative spike timing during sharp-wave ripples was then computed. This subsampling process was repeated 50 times and then averaged across the 50 subsampling events so that each pair had one metric of connection strength. We found similar results using another approach in which we used the original spike trains but then removed cell pairs from the *WT* group in order to match the spike count total of the *5XFAD* group. Across both of these subsampling analyses, we found similar trends as the full dataset.

QUANTIFICATION AND STATISTICAL ANALYSIS

For each of our genotype groups, we had 6-8 animals, 1-4 recording sessions per animal, and many experimental measurements from each animal (e.g., neurons, ripples, time-periods). As a result, we had a hierarchical data structure with many data points that were not independent of each other. To accurately assess the significance of differences between these genotypes without falsely inflating our sample size via pseudoreplication, we used a hierarchical bootstrapping approach (Carpenter et al., 2003; Efron, 1992; Efron and Tibshirani, 1993; Field and Welsh, 2007; Harden, 2011; Saravanan et al., 2020; Thai et al., 2013). In bootstrapping, N subsamples of the dataset are resampled with replacement from the original data and then the metric of interest is calculated for each subsample. This results in a distribution ($n = N$) of values of the metric of interest. To address the non-independence of the hierarchical data, we applied this bootstrapping separately across all of the levels of the hierarchical data. Thus, to calculate a single subsample, we resampled across the following levels: genotype, animal, recording sessions, data point of interest. For each genotype population (*5XFAD* and *WT*), we resampled with replacement from the second level (animals), then for each resampled animal, we resampled with replacement from the next level (sessions), and finally for each session we resampled with replacement from the lowest level (our data point of interest).

To apply this hierarchical bootstrap approach to our statistical analyses, we calculated the direct posterior probabilities for the hypotheses we tested, and thus we reported our results in terms of direct probabilities of the *WT* population being greater than or equal to the *5XFAD* population. This is in contrast to statistical tests such as t tests or ANOVAs, which test whether to reject the null hypothesis and their p values indicate the probability that the null hypothesis is true. We performed the hierarchical bootstrapping as described above, then calculated the mean of this resampled population of values, and then repeated the bootstrapping 10^4 times. We thus produced a distribution of resampled means for each genotype. These resampled distributions were used to compute whether the metric of interest was significantly different between genotypes. To do so, we calculated a joint probability distribution between the bootstrapped means of the *WT* and *5XFAD* groups. The null hypothesis of no difference between the populations would correspond to a circle centered about the unity line. To test the difference between the *WT* and *5XFAD* groups, we compute the volume of the joint probability distribution on one side of the unity line, thus we quantified the probability of the *WT* population of bootstrapped means being greater than or equal to the *5XFAD* population of bootstrapped means. To quantify error accurately given our hierarchical data, we also used the *WT* and *5XFAD* populations of bootstrapped means to quantify standard error of the mean as the 95% confidence interval of the sample of means. Note that for all reports of mean \pm SEM, the mean was calculated from the actual, not-resampled data, and the SEM was generated from the resampled population. These analyses were performed with custom MATLAB and Python scripts. For a few metrics with noticeable outliers, we excluded outliers detected to be greater than 3 scaled median absolute deviations from the median taken from the distribution of all data from both genotypes. The probability is significant if the direct probability supporting the hypothesis, $p < \alpha/2$ or if $p > (1-\alpha/2)$. Throughout the paper, $\text{prob}(WT \geq 5XFAD)$ is used as shorthand to indicate the probability of the resampled mean metric of *WT* mice being greater than or equal to that of the resampled mean of *5XFAD* mice. Significance values are reported as follows: $\text{prob} > 0.95$ or $\text{prob} < 0.05$ ($\alpha = 0.10$, +), $p > 0.975$ or $\text{prob} < 0.025$ ($\alpha = 0.05$, *), $\text{prob} > 0.995$ or $\text{prob} < 0.005$ ($\alpha = 0.01$, **), $\text{prob} > 0.9995$ or $\text{prob} < 0.0005$ ($\alpha = 0.001$, ***). Details on specific statistical parameters are described in the figure legends.

Supplementary Material

Refer to Web version on PubMed Central for supplementary material.

ACKNOWLEDGMENTS

We are grateful to members of the Singer laboratory for technical assistance and comments on the paper. We are also grateful to Bailey Mariner for providing illustrations. This work was supported by NSF GRFP grant DGE-1444932 and NIH grant T32NS096050-22 (to S.M.P.); the Packard Award in Science and Engineering, NIH grant R01-NS109226, Friends and Alumni of Georgia Tech, and the Lane Family (to A.C.S.); and by NIH grant T32 NS007480-18, a Fulton County Elder Health Science Fellowship, and Wright Family (to A.L.P.).

REFERENCES

Abramov E, Dolev I, Fogel H, Ciccotosto GD, Ruff E, and Slutsky I (2009). Amyloid- β as a positive endogenous regulator of release probability at hippocampal synapses. *Nat. Neurosci.* 12, 1567–1576. [PubMed: 19935655]

- Alger BE, and Nicoll RA (1982). Feed-forward dendritic inhibition in rat hippocampal pyramidal cells studied in vitro. *J. Physiol.* 328, 105–123. [PubMed: 7131309]
- Ali F, Baringer SL, Neal A, Choi EY, and Kwan AC (2019). Parvalbumin-positive neuron loss and amyloid- β deposits in the frontal cortex of Alzheimer's disease-related mice. *J. Alzheimers Dis.* 72, 1323–1339. [PubMed: 31743995]
- Alonso JM, Usrey WM, and Reid RC (1996). Precisely correlated firing in cells of the lateral geniculate nucleus. *Nature* 383, 815–819. [PubMed: 8893005]
- Amarasingham A, Harrison MT, Hatsopoulos NG, and Geman S (2012). Conditional modeling and the jitter method of spike resampling. *J. Neurophysiol.* 107, 517–531. [PubMed: 22031767]
- Aronov D, and Tank DW (2014). Engagement of neural circuits underlying 2D spatial navigation in a rodent virtual reality system. *Neuron* 84, 442–456. [PubMed: 25374363]
- Axmacher N, Elger CE, and Fell J (2008). Ripples in the medial temporal lobe are relevant for human memory consolidation. *Brain* 131, 1806–1817. [PubMed: 18503077]
- Barthó P, Hirase H, Monconduit L, Zugaro M, Harris KD, and Buzsáki G (2004). Characterization of neocortical principal cells and interneurons by network interactions and extracellular features. *J. Neurophysiol.* 92, 600–608 [PubMed: 15056678]
- Bartos M, Vida I, Frotscher M, Meyer A, Monyer H, Geiger JRP, and Jonas P (2002). Fast synaptic inhibition promotes synchronized gamma oscillations in hippocampal interneuron networks. *Proc. Natl. Acad. Sci. USA* 99, 13222–13227. [PubMed: 12235359]
- Bartos M, Vida I, and Jonas P (2007). Synaptic mechanisms of synchronized gamma oscillations in inhibitory interneuron networks. *Nat. Rev. Neurosci.* 8, 45–56. [PubMed: 17180162]
- Bero AW, Yan P, Roh JH, Cirrito JR, Stewart FR, Raichle ME, Lee J-M, and Holtzman DM. (2011). Neuronal activity regulates the regional vulnerability to amyloid- β deposition. *Nat. Neurosci.* 14, 750–756. [PubMed: 21532579]
- Braak H, and Braak E (1991). Neuropathological staging of Alzheimer-related changes. *Acta Neuropathol.* 82, 239–259. [PubMed: 1759558]
- Busche MA, Eichhoff G, Adelsberger H, Abramowski D, Wiederhold KH, Haass C, Staufenbiel M, Konnerth A, and Garaschuk O (2008). Clusters of hyperactive neurons near amyloid plaques in a mouse model of Alzheimer's disease. *Science* 321, 1686–1689. [PubMed: 18802001]
- Buskila Y, Crowe SE, and Ellis-Davies GCR (2013). Synaptic deficits in layer 5 neurons precede overt structural decay in 5xFAD mice. *Neuroscience* 254, 152–159. [PubMed: 24055684]
- Buzsáki G (1986). Hippocampal sharp waves: Their origin and significance. *Brain Res.* 398, 242–252. [PubMed: 3026567]
- Buzsáki G (2015). Hippocampal sharp wave-ripple: A cognitive biomarker for episodic memory and planning. *Hippocampus* 25, 1073–1188. [PubMed: 26135716]
- Buzsáki G, Leung LW, and Vanderwolf CH (1983). Cellular bases of hippocampal EEG in the behaving rat. *Brain Res.* 287, 139–171. [PubMed: 6357356]
- Caccavano A, Bozzelli PL, Forcelli PA, Pak DTS, Wu J-Y, Conant K, and Vicini S (2020). Inhibitory parvalbumin basket cell activity is selectively reduced during hippocampal sharp wave ripples in a mouse model of familial Alzheimer's disease. *J. Neurosci.* 40, 5116–5136. [PubMed: 32439703]
- Carpenter JR, Goldstein H, and Rasbash J (2003). A novel bootstrap procedure for assessing the relationship between class size and achievement. *J. R. Stat. Soc. Ser. C Appl. Stat.* 52, 431–443.
- Carr MF, Jadhav SP, and Frank LM (2011). Hippocampal replay in the awake state: a potential substrate for memory consolidation and retrieval. *Nat. Neurosci.* 14, 147–153. [PubMed: 21270783]
- Chapman PF, White GL, Jones MW, Cooper-Blacketer D, Marshall VJ, Irizarry M, Younkin L, Good MA, Bliss TVP, Hyman BT, et al. (1999). Impaired synaptic plasticity and learning in aged amyloid precursor protein transgenic mice. *Nat. Neurosci.* 2, 271–276. [PubMed: 10195221]
- Chung JE, Magland JF, Barnett AH, Tolosa VM, Tooker AC, Lee KY, Shah KG, Felix SH, Frank LM, and Greengard LF (2017). A fully automated approach to spike sorting. *Neuron* 95, 1381–1394.e6. [PubMed: 28910621]
- Coghlan S, Horder J, Inkster B, Mendez MA, Murphy DG, and Nutt DJ (2012). GABA system dysfunction in autism and related disorders: From synapse to symptoms. *Neurosci. Biobehav. Rev.* 36, 2044–2055. [PubMed: 22841562]

- Constantinople CM, and Bruno RM (2011). Effects and mechanisms of wakefulness on local cortical networks. *Neuron* 69, 1061–1068. [PubMed: 21435553]
- Crowe SE, and Ellis-Davies GCR (2014). Spine pruning in 5xFAD mice starts on basal dendrites of layer 5 pyramidal neurons. *Brain Struct. Funct.* 219, 571–580. [PubMed: 23417057]
- Csicsvari J, Hirase H, Czurko A, and Buzsáki G (1998). Reliability and state dependence of pyramidal cell-interneuron synapses in the hippocampus: An ensemble approach in the behaving rat. *Neuron* 21, 179–189. [PubMed: 9697862]
- Csicsvari J, Hirase H, Czurko A, Mamiya A, and Buzsáki G (1999). Oscillatory coupling of hippocampal pyramidal cells and interneurons in the behaving Rat. *J. Neurosci.* 19, 274–287. [PubMed: 9870957]
- Davidson TJ, Kloosterman F, and Wilson MA (2009). Hippocampal replay of extended experience. *Neuron* 63, 497–507. [PubMed: 19709631]
- de Pins B, Cifuentes-Díaz C, Farah AT, López-Molina L, Montalban E, Sancho-Balsells A, López A, Ginés S, Delgado-García JM, Alberch J, et al. (2019). Conditional BDNF delivery from astrocytes rescues memory deficits, spine density, and synaptic properties in the 5xFAD mouse model of alzheimer disease. *J. Neurosci.* 39, 2441–2458. [PubMed: 30700530]
- DeKosky ST, and Scheff SW (1990). Synapse loss in frontal cortex biopsies in Alzheimer's disease: Correlation with cognitive severity. *Ann. Neurol.* 27, 457–464. [PubMed: 2360787]
- Diba K, and Buzsáki G (2007). Forward and reverse hippocampal place-cell sequences during ripples. *Nat. Neurosci.* 10, 1241–1242. [PubMed: 17828259]
- Diba K, Amarasingham A, Mizuseki K, and Buzsáki G (2014). Millisecond timescale synchrony among hippocampal neurons. *J. Neurosci.* 34, 14984–14994. [PubMed: 25378164]
- Dragoi G, and Tonegawa S (2013). Development of schemas revealed by prior experience and NMDA receptor knock-out. *eLife* 2, e01326. [PubMed: 24327561]
- Efron B (1992). Bootstrap methods: Another look at the jackknife. In *Break-throughs in Statistics*, Kotz S and Johnson NL, eds. (Springer), pp. 569–593.
- Efron B, and Tibshirani RJ (1993). *An Introduction to the Bootstrap* (Chapman and Hall).
- English DF, McKenzie S, Evans T, Kim K, Yoon E, and Buzsáki G (2017). pyramidal cell-interneuron circuit architecture and dynamics in hippocampal networks. *Neuron* 96, 505–520.e7. [PubMed: 29024669]
- Fernández-Ruiz A, Oliva A, Oliveira EF, de Rocha-Almeida F, Tingley D, and Buzsáki G (2019). Long-duration hippocampal sharp wave ripples improve memory. *Science* 364, 1082–1086. [PubMed: 31197012]
- Field CA, and Welsh AH (2007). Bootstrapping clustered data. *J. R. Stat. Soc. Ser. B Stat. Methodol.* 69, 369–390.
- Flanigan TJ, Xue Y, Kishan Rao S, Dhanushkodi A, and McDonald MP (2014). Abnormal vibrissa-related behavior and loss of barrel field inhibitory neurons in 5xFAD transgenics. *Genes Brain Behav.* 13, 488–500. [PubMed: 24655396]
- Foster DJ, and Wilson MA (2006). Reverse replay of behavioural sequences in hippocampal place cells during the awake state. *Nature* 440, 680–683. [PubMed: 16474382]
- Freir DB, Holscher C, and Herron CE (2001). Blockade of long-term potentiation by β -amyloid peptides in the CA1 region of the rat hippocampus in vivo. *J. Neurophysiol.* 85, 708–713. [PubMed: 11160505]
- Fujisawa S, Amarasingham A, Harrison MT, and Buzsáki G (2008). Behavior-dependent short-term assembly dynamics in the medial prefrontal cortex. *Nat. Neurosci.* 11, 823–833. [PubMed: 18516033]
- Games D, Adams D, Alessandrini R, Barbour R, Berthelette P, Blackwell C, Carr T, Clemens J, Donaldson T, Gillespie F, et al. (1995). Alzheimer-type neuropathology in transgenic mice overexpressing V717F β -am-yloid precursor protein. *Nature* 373, 523–527. [PubMed: 7845465]
- Geiller T, Fattahi M, Choi JS, and Royer S (2017). Place cells are more strongly tied to landmarks in deep than in superficial CA1. *Nat. Commun.* 8, 14531. [PubMed: 28218283]
- Giesers NK, and Wirths O (2020). Loss of hippocampal calretinin and parvalbumin interneurons in the 5XFAD mouse model of Alzheimer's disease. *ASN Neuro* 12, 1759091420925356. [PubMed: 32423230]

- Gillespie AK, Jones EA, Lin YH, Karlsson MP, Kay K, Yoon SY, Tong LM, Nova P, Carr JS, Frank LM, et al. (2016). Apolipoprotein E4 causes age-dependent disruption of slow gamma oscillations during hippocampal sharp-wave ripples. *Neuron* 90, 740–751. [PubMed: 27161522]
- Girardeau G, and Zugaro M (2011). Hippocampal ripples and memory consolidation. *Curr. Opin. Neurobiol.* 21, 452–459. [PubMed: 21371881]
- Girardeau G, Benchenane K, Wiener SI, Buzsáki G, and Zugaro MB (2009). Selective suppression of hippocampal ripples impairs spatial memory. *Nat. Neurosci.* 12, 1222–1223. [PubMed: 19749750]
- Gonzalez-Burgos G, and Lewis DA (2008). GABA neurons and the mechanisms of network oscillations: implications for understanding cortical dysfunction in schizophrenia. *Schizophr. Bull.* 34, 944–961. [PubMed: 18586694]
- Haider B, Häusser M, and Carandini M (2013). Inhibition dominates sensory responses in the awake cortex. *Nature* 493, 97–100. [PubMed: 23172139]
- Harden JJ (2011). A bootstrap method for conducting statistical inference with clustered data. *State Polit. Policy Q.* 11, 223–246.
- Hatsopoulos N, Geman S, Amarasingham A, and Bienenstock E (2003). At what time scale does the nervous system operate? *Neurocomputing* 52-54, 25–29.
- Hsia AY, Masliah E, McConlogue L, Yu GQ, Tatsuno G, Hu K, Kholodenko D, Malenka RC, Nicoll RA, and Mucke L (1999). Plaque-independent disruption of neural circuits in Alzheimer's disease mouse models. *Proc. Natl. Acad. Sci. USA* 96, 3228–3233. [PubMed: 10077666]
- Iaccarino HF, Singer AC, Martorell AJ, Rudenko A, Gao F, Gillingham TZ, Mathys H, Seo J, Kritskiy O, Abdurrob F, et al. (2016). Gamma frequency entrainment attenuates amyloid load and modifies microglia. *Nature* 540, 230–235. [PubMed: 27929004]
- Isaacson JS, and Scanziani M (2011). How inhibition shapes cortical activity. *Neuron* 72, 231–243. [PubMed: 22017986]
- Jackson JC, Johnson A, and Redish AD (2006). Hippocampal sharp waves and reactivation during awake states depend on repeated sequential experience. *J. Neurosci.* 26, 12415–12426. [PubMed: 17135403]
- Jadhav SP, Kemere C, German PW, and Frank LM (2012). Awake hippocampal sharp-wave ripples support spatial memory. *Science* 336, 1454–1458. [PubMed: 22555434]
- Jones EA, Gillespie AK, Yoon SY, Frank LM, and Huang Y (2019). Early hippocampal sharp-wave ripple deficits predict later learning and memory impairments in an Alzheimer's disease mouse model. *Cell Rep.* 29, 2123–2133.e4. [PubMed: 31747587]
- Karlsson MP, and Frank LM (2009). Awake replay of remote experiences in the hippocampus. *Nat. Neurosci.* 12, 913–918. [PubMed: 19525943]
- Kimura R, and Ohno M (2009). Impairments in remote memory stabilization precede hippocampal synaptic and cognitive failures in 5XFAD Alzheimer mouse model. *Neurobiol. Dis.* 33, 229–235. [PubMed: 19026746]
- Klausberger T, Magill PJ, Márton LF, Roberts JDB, Cobden PM, Buzsáki G, and Somogyi P (2003). Brain-state- and cell-type-specific firing of hippocampal interneurons in vivo. *Nature* 421, 844–848. [PubMed: 12594513]
- Langston RF, Ainge JA, Couey JJ, Canto CB, Bjerknes TL, Witter MP, Moser EI, and Moser MB (2010). Development of the spatial representation system in the rat. *Science* 328, 1576–1580. [PubMed: 20558721]
- Leung L, Andrews-Zwilling Y, Yoon SY, Jain S, Ring K, Dai J, Wang MM, Tong L, Walker D, and Huang Y (2012). Apolipoprotein E4 causes age- and sex-dependent impairments of hilar GABAergic interneurons and learning and memory deficits in mice. *PLoS One* 7, e53569. [PubMed: 23300939]
- Li G, Bien-Ly N, Andrews-Zwilling Y, Xu Q, Bernardo A, Ring K, Halabisky B, Deng C, Mahley RW, and Huang Y (2009). GABAergic interneuron dysfunction impairs hippocampal neurogenesis in adult apolipoprotein E4 knockin mice. *Cell Stem Cell* 5, 634–635. [PubMed: 19951691]
- Martinez-Losa M, Tracy TE, Ma K, Verret L, Clemente-Perez A, Khan AS, Cobos I, Ho K, Gan L, Mucke L, et al. (2018). Nav1.1-overexpressing interneuron transplants restore brain rhythms and cognition in a mouse model of Alzheimer's disease. *Neuron* 98, 75–89.e5. [PubMed: 29551491]

- Martorell AJ, Paulson AL, Suk H-J, Abdurrob F, Drummond GT, Guan W, Young JZ, Kim DN-W, Kritskiy O, Barker SJ, et al. (2019). Multi-sensory gamma stimulation ameliorates Alzheimer's-associated pathology and improves cognition. *Cell* 177, 256–271.e22. [PubMed: 30879788]
- Niell CM, and Stryker MP (2008). Highly selective receptive fields in mouse visual cortex. *J. Neurosci.* 28, 7520–7536. [PubMed: 18650330]
- O'Leary TP, Robertson A, Chipman PH, Rafuse VF, and Brown RE (2018). Motor function deficits in the 12 month-old female 5xFAD mouse model of Alzheimer's disease. *Behav. Brain Res.* 337, 256–263. [PubMed: 28890389]
- O'Neill J, Senior TJ, Allen K, Huxter JR, and Csicsvari J (2008). Reactivation of experience-dependent cell assembly patterns in the hippocampus. *Nat. Neurosci.* 11, 209–215. [PubMed: 18193040]
- Oakley H, Cole SL, Logan S, Maus E, Shao P, Craft J, Guillozet-Bongaarts A, Ohno M, Disterhoft J, Van Eldik L, et al. (2006). Intraneuronal β -amyloid aggregates, neurodegeneration, and neuron loss in transgenic mice with five familial Alzheimer's disease mutations: potential factors in amyloid plaque formation. *J. Neurosci.* 26, 10129–10140. [PubMed: 17021169]
- Palop JJ, and Mucke L (2010). Amyloid- β -induced neuronal dysfunction in Alzheimer's disease: from synapses toward neural networks. *Nat. Neurosci.* 13, 812–818. [PubMed: 20581818]
- Palop JJ, and Mucke L (2016). Network abnormalities and interneuron dysfunction in Alzheimer disease. *Nat. Rev. Neurosci.* 17, 777–792. [PubMed: 27829687]
- Palop JJ, Chin J, Roberson ED, Wang J, Thwin MT, Bien-Ly N, Yoo J, Ho KO, Yu GQ, Kreitzer A, et al. (2007). Aberrant excitatory neuronal activity and compensatory remodeling of inhibitory hippocampal circuits in mouse models of Alzheimer's disease. *Neuron* 55, 697–711. [PubMed: 17785178]
- Perkel DH, Gerstein GL, and Moore GP (1967). Neuronal spike trains and stochastic point processes: ii. simultaneous spike trains. *Biophys. J.* 7, 419–440. [PubMed: 4292792]
- Petrache AL, Rajulawalla A, Shi A, Wetzel A, Saito T, Saido TC, Harvey K, and Ali AB (2019). Aberrant excitatory-inhibitory synaptic mechanisms in entorhinal cortex microcircuits during the pathogenesis of Alzheimer's disease. *Cereb. Cortex* 29, 1834–1850. [PubMed: 30766992]
- Pfeiffer BE, and Foster DJ (2013). Hippocampal place-cell sequences depict future paths to remembered goals. *Nature* 497, 74–79. [PubMed: 23594744]
- Ponomarenko AA, Korotkova TM, Sergeeva OA, and Haas HL (2004). Multiple GABAA receptor subtypes regulate hippocampal ripple oscillations. *Eur. J. Neurosci.* 20, 2141–2148. [PubMed: 15450093]
- Pouille F, and Scanziani M (2001). Enforcement of temporal fidelity in pyramidal cells by somatic feed-forward inhibition. *Science* 293, 1159–1163. [PubMed: 11498596]
- Puzzo D, Privitera L, Leznik E, Fà M, Staniszewski A, Palmeri A, and Arancio O (2008). Picomolar amyloid- β positively modulates synaptic plasticity and memory in hippocampus. *J. Neurosci.* 28, 14537–14545 [PubMed: 19118188]
- Ravassard P, Kees A, Willers B, Ho D, Aharoni D, Cushman J, Aghajan ZM, and Mehta MR (2013). Multisensory control of hippocampal spatiotemporal selectivity. *Science* 340, 1342–1346. [PubMed: 23641063]
- Reid RC, and Alonso JM (1995). Specificity of monosynaptic connections from thalamus to visual cortex. *Nature* 378, 281–284. [PubMed: 7477347]
- Saravanan V, Berman GJ, and Sober SJ (2020). Application of the hierarchical bootstrap to multi-level data in neuroscience. *Neuron. Behav. DataAnal. Theory*, Published online July 21, 2020.
- Scarce-Levie K, Sanchez PE, and Lewcock JW (2020). Leveraging pre-clinical models for the development of Alzheimer disease therapeutics. *Nat. Rev. Drug Discov.* 19, 447–462. [PubMed: 32612262]
- Schlinghoff D, Káli S, Freund TF, Hájos N, and Gulyás AI (2014). Mechanisms of sharp wave initiation and ripple generation. *J. Neurosci.* 34, 11385–11398. [PubMed: 25143618]
- Schneider F, Baldauf K, Wetzel W, and Reymann KGG (2014). Behavioral and EEG changes in male 5xFAD mice. *Physiol. Behav.* 135, 25–33. [PubMed: 24907698]
- Selkoe DJ (2002). Alzheimer's disease is a synaptic failure. *Science* 298, 789–791. [PubMed: 12399581]

- Senzai Y, Fernandez-Ruiz A, and Buzsáki G (2019). Layer-specific physiological features and interlaminar interactions in the primary visual cortex of the mouse. *Neuron* 101, 500–513.e5. [PubMed: 30635232]
- Singer AC, and Frank LM (2009). Rewarded outcomes enhance reactivation of experience in the hippocampus. *Neuron* 64, 910–921. [PubMed: 20064396]
- Singer AC, Carr MF, Karlsson MP, and Frank LM (2013). Hippocampal SWR activity predicts correct decisions during the initial learning of an alternation task. *Neuron* 77, 1163–1173. [PubMed: 23522050]
- Skaggs WE, McNaughton BL, Wilson MA, and Barnes CA (1996). Theta phase precession in hippocampal neuronal populations and the compression of temporal sequences. *Hippocampus* 6, 149–172. [PubMed: 8797016]
- Staresina BP, Bergmann TO, Bonnefond M, van der Meij R, Jensen O, Deuker L, Elger CE, Axmacher N, and Fell J (2015). Hierarchical nesting of slow oscillations, spindles and ripples in the human hippocampus during sleep. *Nat. Neurosci.* 18, 1679–1686. [PubMed: 26389842]
- Stark E, Roux L, Eichler R, Senzai Y, Royer S, and Buzsáki G (2014). Pyramidal cell-interneuron interactions underlie hippocampal ripple oscillations. *Neuron* 83, 467–480. [PubMed: 25033186]
- Stella F, Baracska P, O'Neill J, and Csicsvari J (2019). Hippocampal reactivation of random trajectories resembling Brownian diffusion. *Neuron* 102, 450–461.e7. [PubMed: 30819547]
- Stéphan A, Laroche S, and Davis S (2001). Generation of aggregated β -amyloid in the rat hippocampus impairs synaptic transmission and plasticity and causes memory deficits. *J. Neurosci.* 21, 5703–5714. [PubMed: 11466442]
- Stephan KE, Baldeweg T, and Friston KJ (2006). Synaptic plasticity and dysconnection in schizophrenia. *Biol. Psychiatry* 59, 929–939. [PubMed: 16427028]
- Steriade M, Timofeev I, and Grenier F (2001). Natural waking and sleep states: A view from inside neocortical neurons. *J. Neurophysiol.* 85, 1969–1985. [PubMed: 11353014]
- Suh J, Foster DJ, Davoudi H, Wilson MA, and Tonegawa S (2013). Impaired hippocampal ripple-associated replay in a mouse model of schizophrenia. *Neuron* 80, 484–493. [PubMed: 24139046]
- Tanaka K (1983). Cross-correlation analysis of geniculostriate neuronal relationships in cats. *J. Neurophysiol.* 49, 1303–1318. [PubMed: 6875624]
- Terry RD (2000). Cell death or synaptic loss in Alzheimer disease. *J. Neuropathol. Exp. Neurol.* 59, 1118–1119. [PubMed: 11138931]
- Terry RD, Masliah E, Salmon DP, Butters N, DeTeresa R, Hill R, Hansen LA, and Katzman R (1991). Physical basis of cognitive alterations in Alzheimer's disease: Synapse loss is the major correlate of cognitive impairment. *Ann. Neurol.* 30, 572–580. [PubMed: 1789684]
- Thai HT, Mentré F, Holford NHG, Veyrat-Follet C, and Comets E (2013). A comparison of bootstrap approaches for estimating uncertainty of parameters in linear mixed-effects models. *Pharm. Stat.* 12, 129–140. [PubMed: 23457061]
- Toyama K, Kimura M, and Tanaka K (1981). Organization of cat visual cortex as investigated by cross-correlation technique. *J. Neurophysiol.* 46, 202–214. [PubMed: 6267212]
- Usrey WM, Reppas JB, and Reid RC (1999). Specificity and strength of retinogeniculate connections. *J. Neurophysiol.* 82, 3527–3540. [PubMed: 10601479]
- van Spronsen M, and Hoogenraad CC (2010). Synapse pathology in psychiatric and neurologic disease. *Curr. Neurol. Neurosci. Rep.* 10, 207–214. [PubMed: 20425036]
- Vaz AP, Inati SK, Brunel N, and Zaghoul KA (2019). Coupled ripple oscillations between the medial temporal lobe and neocortex retrieve human memory. *Science* 363, 975–978. [PubMed: 30819961]
- Verret L, Mann EO, Hang GB, Barth AMI, Cobos I, Ho K, Devidze N, Masliah E, Kreitzer AC, Mody I, et al. (2012). Inhibitory interneuron deficit links altered network activity and cognitive dysfunction in Alzheimer model. *Cell* 149, 708–721. [PubMed: 22541439]
- Vizuete JA, Pillay S, Diba K, Ropella KM, and Hudetz AG (2012). Monosynaptic functional connectivity in cerebral cortex during wakefulness and under graded levels of anesthesia. *Front. Integr. Neurosci.* 6, 90. [PubMed: 23091451]

- Walsh DM, Klyubin I, Fadeeva JV, Cullen WK, Anwyl R, Wolfe MS, Rowan MJ, and Selkoe DJ (2002). Naturally secreted oligomers of amyloid β protein potently inhibit hippocampal long-term potentiation in vivo. *Nature* 416,535–539. [PubMed: 11932745]
- Wilson MA, and McNaughton BL (1994). Reactivation of hippocampal ensemble memories during sleep. *Science* 265, 676–679. [PubMed: 8036517]
- Xiao NA, Zhang J, Zhou M, Wei Z, Wu XL, Dai XM, Zhu YG, and Chen XC (2015). Reduction of glucose metabolism in olfactory bulb is an earlier Alzheimer’s disease-related biomarker in 5XFAD mice. *Chin. Med. J. (Engl.)* 128, 2220–2227. [PubMed: 26265617]
- Ylinen A, Bragin A, Nádasdy Z, Jandó G, Szabó I, Sik A, and Buzsáki G (1995). Sharp wave-associated high-frequency oscillation (200 Hz) in the intact hippocampus: Network and intracellular mechanisms. *J. Neurosci.* 15, 30–46. [PubMed: 7823136]

Highlights

- *5XFAD* mice have weakened inhibitory synaptic efficacy during behavior
- Weakened inhibition in *5XFAD* mice occurs during sharp-wave ripples
- *5XFAD* mice have fewer and shorter sharp-wave ripples
- Place cell reactivation is impaired during the remaining ripples in *5XFAD* mice

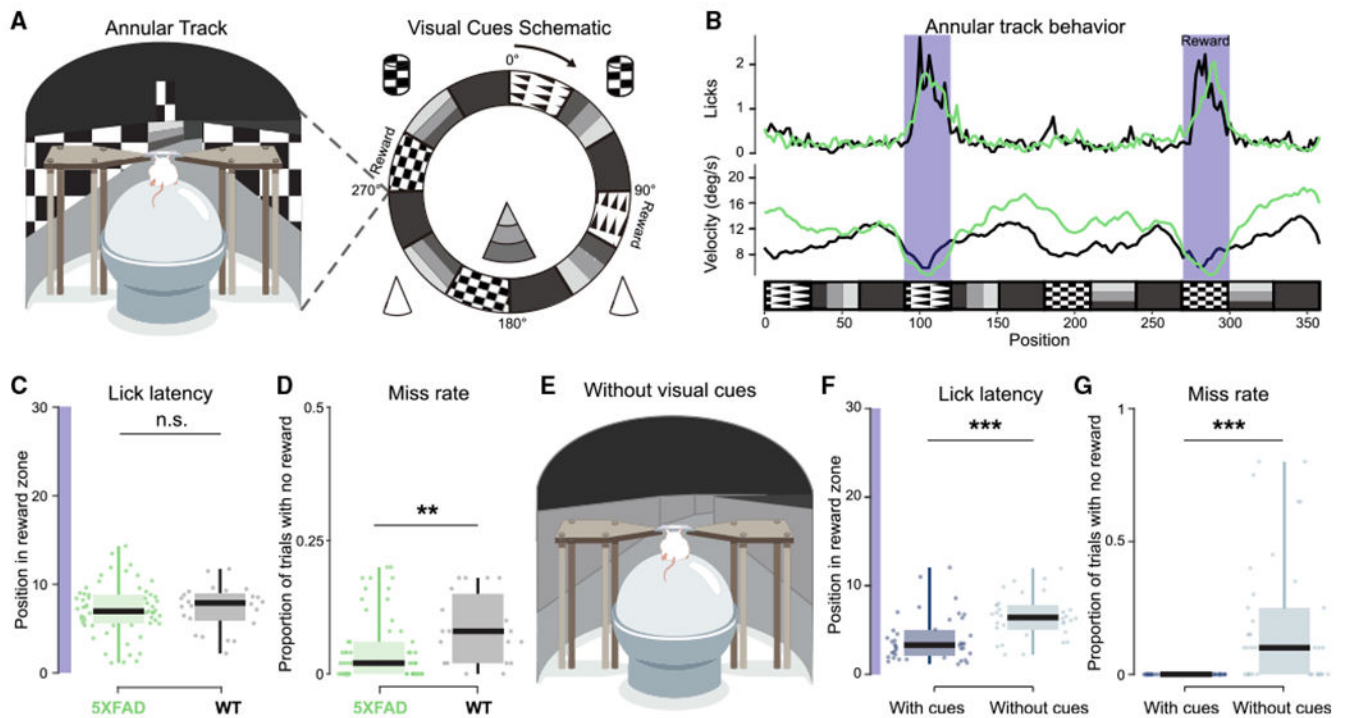


Figure 1. 5XFAD mice and wild-type (WT) littermates lick for reward in a virtual reality spatial task

(A) Left: schematic of virtual reality experimental setup. Right: annular track spatial navigation task with local and distal cues.

(B) Example of lick and velocity rate averaged over 50 trials of 5XFAD (green) and WT (black) mice as a function of position in the annular track. Each trial is considered one lap around the annular track. Reward zones are indicated in dark purple.

(C) Lick latency (position at the first lick after reward zone entry) for 50-trial blocks for all sessions in 5XFAD (green) and WT (black) mice from the start of the reward zone (degree 0) to the end of the reward zone (degree 30) on trials when the animal received a reward. Dot indicates 50-trial block. Purple highlight indicates length of reward zone. 5XFAD, 7.13 ± 0.72 degrees, $n = 8$ animals; WT, 7.38 ± 1.01 degrees, $n = 4$ animals (only including animals with >50 trials); $\text{prob}(\text{WT} < 5XFAD) = 0.64$; 5XFAD, $n = 59$ trial blocks, lick latency percentiles = 1.12, 5.59, 6.95, 8.82, 14.32; WT, $n = 24$ trial blocks, lick latency percentiles = 2.19, 6.01, 7.90, 8.91, 11.74.

(D) Miss rate (number of laps around the annular track with zero rewards received) for 50-trial blocks for all sessions in 5XFAD (green) and WT (black) mice. Each dot indicates a 50-trial-block, 5XFAD, $4.3\% \pm 1.46\%$ trials with zero rewards; WT, $8.4\% \pm 2.72\%$; $\text{prob}(\text{WT} < 5XFAD) = 0.996^{**}$; 5XFAD, $n = 60$ trial blocks, miss rate percentiles = 0, 0, 0.02, 0.060, 0.20; WT, $n = 19$ trial blocks, miss rate percentiles = 0, 0.02, 0.08, 0.14, 0.18.

(E) Annular track spatial navigation task with visual cues removed.

(F) As in (C) for track with and without visual cues. Dark blue indicates data from last two sessions in the annular track with visual cues, and light blue indicates the first two sessions in the annular track without visual cues. Track with cues: 5XFAD, 5.63 ± 1.37 ; WT, 3.02 ± 0.56 ; track without cues: 5XFAD, 7.65 ± 0.69 ; WT, 4.99 ± 0.14 ; $\text{prob}(\text{with cues} < \text{without}$

cues) $< 10^{-4}$ (limit due to resampling 10^4 times)***; with visual cues: *5XFAD*, $n = 3$ animals, lick latency percentiles = 2.46, 3.30, 4.95, 6.94, 12.06; WT, $n = 3$ animals, lick latency percentiles = 1.14, 1.68, 2.44, 3.50; without visual cues: *5XFAD*, $n = 3$ animals, lick latency percentiles = 6.89, 6.97, 7.22, 7.60, 9.56; WT, $n = 3$ animals, lick latency percentiles = 3.15, 3.58, 4.57, 6.34, 7.48.

(G) As in (D) for track with visual cues (dark blue) versus the track without visual cues (light blue) in *5XFAD* and WT mice. Track with cues: *5XFAD*, 0 ± 0 , WT, 0 ± 0 miss trials; track without cues: *5XFAD*, $34.5\% \pm 0.19\%$ miss trials; WT, $40.22\% \pm 0.32\%$ miss trials; $\text{prob}(\text{with cues} > \text{without cues}) < 10^{-4}$ (limit due to resampling 10^4 times)***; with visual cues: *5XFAD*, $n = 3$ animals, miss rate percentiles = 0, 0, 0, 0, 0; WT, $n = 2$ animals, miss rate percentiles = 0, 0, 0, 0, 0; without visual cues: *5XFAD*, $n = 3$ animals, miss rate percentiles = 6.89, 6.97, 7.22, 7.60, 9.56; WT, $n = 3$ animals, miss rate percentiles = 3.15, 3.58, 4.57, 6.34, 7.47. See also Figure S1. Boxplot edges indicate quartiles, whiskers indicate range, and black bar indicates median. All percentiles are minimum, 25th percentile, median, 75th percentile, maximum. All statistics were performed with a hierarchical bootstrap analysis to determine the direct probability that the resampled mean of WT mice is greater than the resampled mean of *5XFAD* mice, in contrast to statistical methods that test whether to reject the null hypothesis. Using this method the probability that WT mice have significantly larger resampled means than do *5XFAD* mice is indicated by $\text{prob}(\text{WT} > \text{5XFAD}) > 0.975$, or $\text{prob} > 1 - \alpha/2$ where α is the significance level. The probability that WT mice have significantly smaller resampled means than do *5XFAD* mice is indicated by $\text{prob}(\text{WT} < \text{5XFAD}) < 0.025$, or $\text{prob} < \alpha/2$ (see STAR Methods). ** $\text{prob} > 0.995$ or $\text{prob} < 0.005$ ($\alpha = 0.01$); *** $\text{prob} > 0.9995$ or $\text{prob} < 0.0005$ ($\alpha = 0.001$); n.s., not significant.

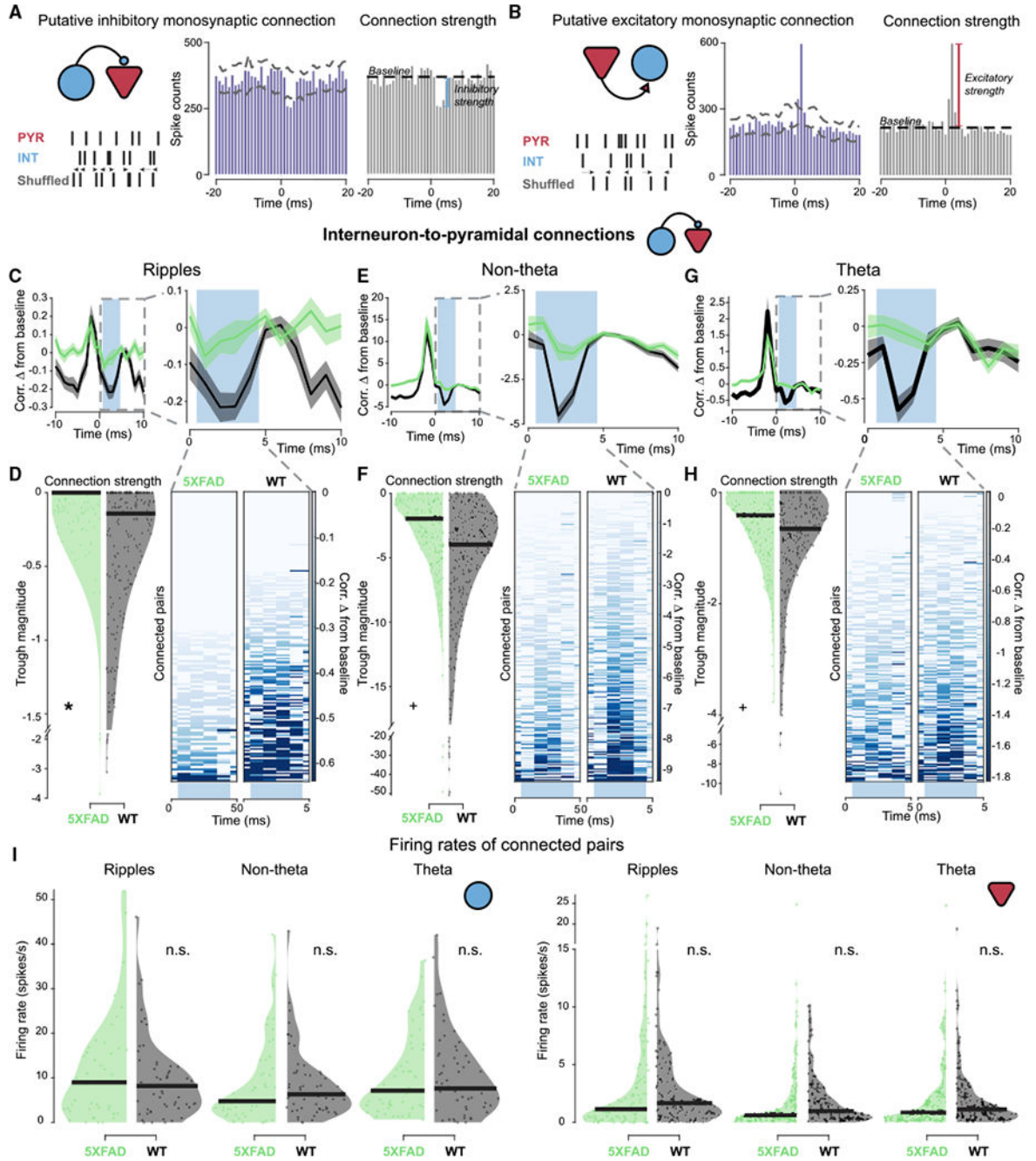


Figure 2. Interneuron-to-pyramidal (INT-to-PYR) monosynaptic connections are weaker in 5XFAD mice

(A) Schematic of monosynaptic connection identification analysis and quantification of inhibitory connection strength. Left: connection type and illustration of shuffled spike train controls. (Center) Example of putative INT-to-PYR connection with cross-correlation values from -20- to +20-ms lags; dashed lines indicate the maximum and minimum values of the cross-correlation of shuffle controls. Connections were identified by a significant trough below the shuffle controls in the 1- to 3-ms range. Right: schematic of inhibitory connection

strength: baseline (an average taken outside the 1- to 4-ms window) minus the trough (minimum value in the 1- to 4-ms window) of the cross-correlogram (CCG).

(B) As in (A) for excitatory connection strength of a PYR-to-INT connection.

(C) Left: average CCG of monosynaptically connected INT-to-PYR cell pairs between *5XFAD* (green) and WT (black) mice during sharp-wave ripple (SWR) periods from -10- to +10-ms lags normalized by geometric mean firing rate and displayed as difference from baseline, mean \pm SEM. Right: zoomed-in view of average CCG on left from 0 to 10-s lag. Light blue box indicates region where connection strength was measured. Inhibitory connection strength was measured as the minimum value in the 1- to 4-ms window. The CCGs that were rectified for the strength measurement are not included in the visualization of the average and individual CCGs. Statistics are described in (D).

(D) Connection strength as measured by trough magnitude in *5XFAD* and WT mice during SWR periods. Each dot indicates the connection strength measured from a single INT-to-PYR cell pair-across all SWR periods. (Right) individual CCGs of putative INT-to-PYR cell connected pairs during SWR periods that make up the average shown above in (C). Heatmap indicates change in correlation from baseline measurement. Note CCGs during SWRs look more variable because there are fewer spikes during SWRs than during non-theta and theta periods. The number of spikes included in this figure was 49,649 in *5XFAD* mice and 167,402 in WT mice. *5XFAD*, -0.14 ± 0.13 trough magnitude; WT, -0.38 ± 0.19 trough magnitude; $\text{prob}(5XFAD < WT) = 0.981^*$, here *5XFAD* < WT indicates a deficit in inhibition because inhibitory troughs are negative; *5XFAD*, $n = 146$ INT-to-PYR cell pairs; connection strength percentiles = $-3.86, -0.13, 0, 0, 0$; WT, $n = 213$ INT-to-PYR cell pairs; connection strength percentiles = $-3.12, -0.59, -0.14, 0, 0$.

(E) As in (C) for INT-to-PYR connections during non-theta periods. Statistics are described in (F).

(F) As in (D) for INT-to-PYR connections during non-theta periods. The number of spikes included in this figure was 12,201,118 in *5XFAD* mice and 15,240,501 in WT mice. *5XFAD*, -3.25 ± 1.04 trough magnitude; WT, -5.78 ± 2.61 trough magnitude; $\text{prob}(5XFAD < WT) = 0.954^+$; *5XFAD*, $n = 250$ INT-to-PYR cell pairs, connection strength percentiles = $-49.17, -4.35, -1.96, -0.59, 0$; WT, $n = 249$ INT-to-PYR cell pairs, connection strength percentiles = $-50.78, -7.46, -3.98, -1.88, 0$.

(G) As in (C) for INT-to-PYR connections during theta periods. Statistics are described in (H).

(H) As in (D) for INT-to-PYR connections during theta periods. The number of spikes included in this figure was 1,122,202 in *5XFAD* mice and 1,451,377 in WT mice. *5XFAD*, -0.61 ± 0.22 trough magnitude; WT, -0.99 ± 0.44 trough magnitude; $\text{prob}(5XFAD < WT) = 0.952^+$; *5XFAD*, $n = 257$ INT-to-PYR cell pairs, connection strength percentiles = $-3.77, -0.93, -0.41, 0, 0$; WT, $n = 244$ INT-to-PYR cell pairs, connection strength percentiles = $-11.06, -1.29, -0.65, -0.25, 0$.

(I) Firing rates for putative INT-to-PYR cell connected pairs during the time periods of interest in *5XFAD* (green) versus WT (black) mice. (Left) Firing rates of pre-synaptic interneurons during time periods of interest; a single dot represents one single unit even when it is part of multiple cell pairs. During ripples: *5XFAD*, 11.66 ± 4.50 Hz; WT, 9.67 ± 2.91 ; $\text{prob}(WT < 5XFAD) = 0.24$; *5XFAD*, 43 interneurons, firing rate percentiles = $0, 3.00, 9.00, 16.48, 51.95$; WT, $n = 56$ interneurons, firing rate percentiles = $0, 3.52, 8.20, 12.53,$

46.12; non-theta: *5XFAD*, 8.59 ± 3.14 ; WT, 8.43 ± 2.53 ; $\text{prob}(\text{WT} > \text{5XFAD}) = 0.46$; *5XFAD*, $n = 54$ interneurons, firing rate percentiles = 0, 2.71, 4.78, 11.87, 42.16; WT, $n = 59$ interneurons, firing rate percentiles = 0, 3.05, 6.32, 11.00, 42.92; theta: *5XFAD*, 10.27 ± 2.74 ; WT, 10.53 ± 2.95 , $\text{prob}(\text{WT} > \text{5XFAD}) = 0.54$; *5XFAD*, $n = 54$ interneurons, firing rate percentiles = 0.62, 3.72, 7.11, 15.62, 36.32; WT, $n = 59$ interneurons, firing rate percentiles = 0, 3.61, 7.65, 14.96, 42.01. (Right) Firing rates of post-synaptic pyramidal cells during time periods of interest. During ripples: *5XFAD*, 3.17 ± 1.78 ; WT, 2.80 ± 0.65 , $\text{prob}(\text{WT} > \text{5XFAD}) = 0.38$; *5XFAD*, $n = 108$ pyramidal cells, firing rate percentiles = 0, 0.36, 1.14, 3.94, 26.97; WT, $n = 131$ pyramidal cells, firing rate percentiles = 0, 0.60, 1.67, 3.75, 18.98; non-theta: *5XFAD*, 1.78 ± 0.64 ; WT, 1.96 ± 0.43 ; $\text{prob}(\text{WT} > \text{5XFAD}) = 0.72$; *5XFAD*, $n = 175$ pyramidal cells, firing rate percentiles = 0, 0.27, 0.61, 2.01, 24.79; WT, $n = 161$ pyramidal cells, firing rate percentiles = 0, 0.34, 0.98, 2.68, 10.16; theta: *5XFAD*, 2.01 ± 0.68 ; WT, 1.95 ± 0.56 ; $\text{prob}(\text{WT} > \text{5XFAD}) = 0.47$; *5XFAD*, $n = 171$ pyramidal cells, firing rate percentiles = 0, 0.24, 0.82, 2.39, 24.53; WT, $n = 160$ pyramidal cells, firing rate percentiles = 0, 0.41, 1.09, 2.41, 18.80.

See also Figures S2, S3, and S5. Black bar indicates median for violin plots. All percentiles are minimum, 25th percentile, median, 75th percentile, maximum. ⁺prob > 0.95 or prob < 0.05 ($\alpha = 0.10$); *p > 0.975 or prob < 0.025 ($\alpha = 0.05$); n.s., not significant throughout as tested by the hierarchical bootstrap analysis, which directly tests the hypothesis that the resampled means differ instead of the likelihood that the null hypothesis should be rejected.

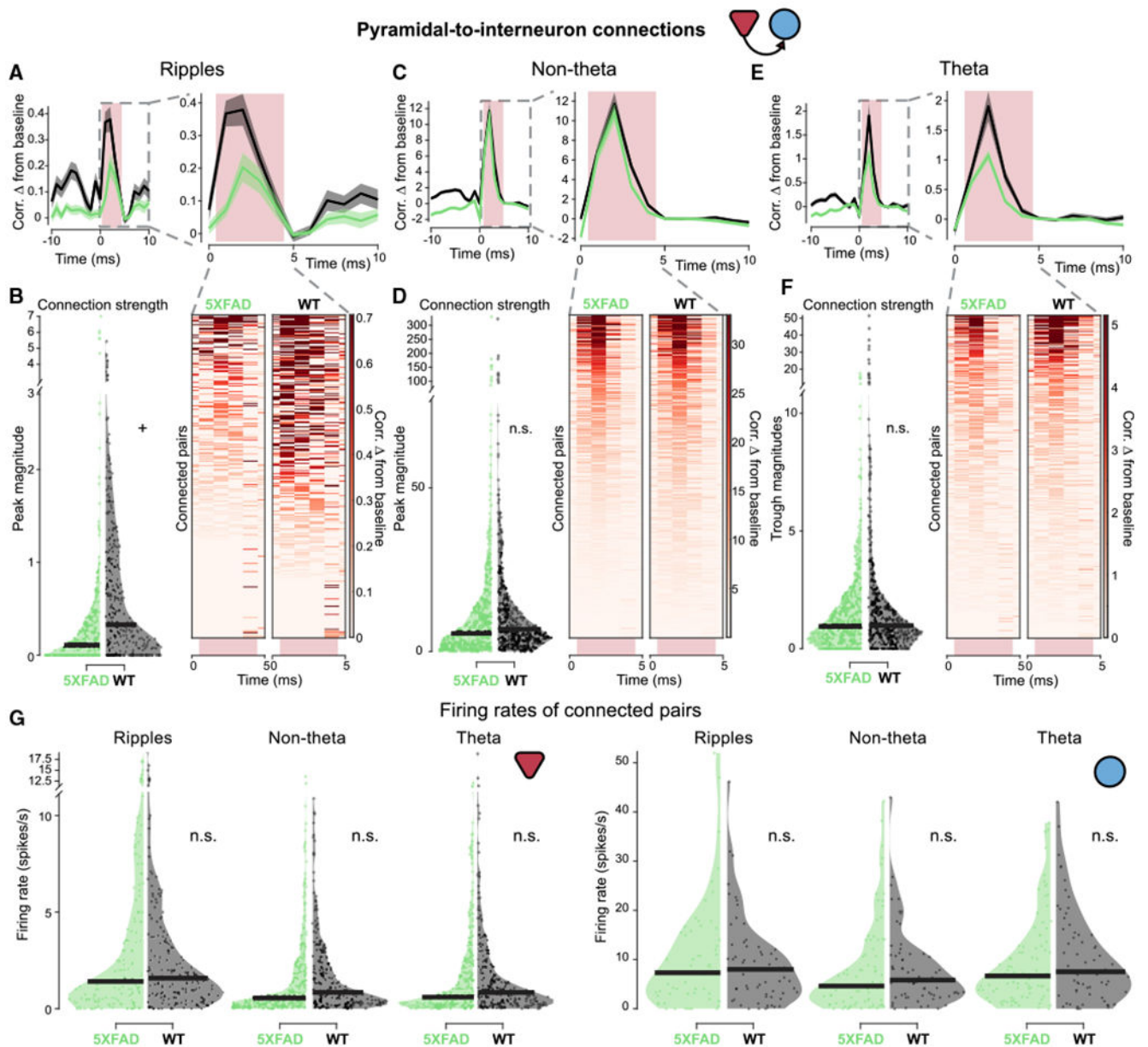


Figure 3. PYR-to-INT monosynaptic connections in 5XFAD mice

(A) (Left) Average cross-correlogram (CCG) of monosynaptically connected PYR-to-INT cell pairs between 5XFAD (green) and WT (black) mice during SWR periods from -10 - to $+10$ -ms lags. Normalized by geometric mean firing rate and displayed as difference from baseline, mean \pm SEM. (Right) View of average CCG on left from 0 to 10-ms lag. Light pink box indicates region where connection strength was measured. Excitatory connection strength was measured as the maximum value in the 1- to 4-ms window. Statistics are described in (B).

(B) Left: connection strength as measured by peak magnitude in 5XFAD and WT mice during SWR periods. Dot indicates the connection strength measured from a single PYR-to-INT cell pair across all SWR periods. Right: individual CCGs of putative PYR-to-INT cell

connected pairs during SWR periods. The individual CCGs make up the average shown above. Heatmap indicates change in correlation from baseline measurement. Note CCGs during SWRs look more variable because there are significantly fewer spikes during SWRs than during non-theta and theta periods. The number of spikes included in this figure was 116,444 in *5XFAD* mice and 243,457 in WT mice. *5XFAD*, 0.36 ± 0.28 peak magnitude; WT, 0.70 ± 0.24 peak magnitude; $\text{prob}(\text{WT} > \text{5XFAD}) = 0.96^+$; *5XFAD*, $n = 306$ PYR-to-INT cell pairs, connection strength percentiles = 0, 0, 0.12, 0.35, 7.01; WT, $n = 349$ PYR-to-INT cell pairs, connection strength percentiles = 0, 0, 0.32, 1.11, 5.40 (minimum, 25th percentile, median, 75th percentile, and maximum, respectively).

(C) As in (A) for PYR-to-INT connections during non-theta periods. Statistics are described in (D).

(D) As in (B) for PYR-to-INT connections during non-theta periods. The number of spikes included in this figure was 12,201,118 in *5XFAD* mice and 21,369,627 in WT mice. *5XFAD*, 12.70 ± 5.35 peak magnitude; WT, 13.81 ± 6.08 peak magnitude; $\text{prob}(\text{WT} > \text{5XFAD}) = 0.62$; *5XFAD*, $n = 527$ PYR-to-INT cell pairs, connection strength percentiles = 0, 1.91, 5.55, 13.61, 330.81; WT, $n = 447$ PYR-to-INT cell pairs, connection strength percentiles = 0, 3.51, 6.78, 13.89, 323.36.

(E) As in (A) for PYR-to-INT connections during theta periods. Statistics are described in (F).

(F) As in (B) for PYR-to-INT connections during theta periods. The number of spikes included in this figure was 2,362,729 in *5XFAD* mice and 2,258,135 in WT mice. *5XFAD*, 1.51 ± 0.54 peak magnitude; WT, 2.32 ± 1.32 peak magnitude; $\text{prob}(\text{WT} > \text{5XFAD}) = 0.89$; *5XFAD*, $n = 539$ PYR-to-INT cell pairs, connection strength percentiles = 0, 0.36, 0.95, 1.93, 17.53; WT, $n = 442$ PYR-to-INT cell pairs, connection strength percentiles = 0, 0.52, 1.00, 1.99, 51.43.

(G) Firing rates for putative PYR-to-INT cell connected pairs during the time periods of interest in *5XFAD* (green) versus WT (black) mice. (Left) firing rates of pre-synaptic pyramidal cells during time periods of interest, each single unit is represented once even when it is part of multiple cell pairs. During ripples: *5XFAD*, 3.35 ± 1.42 ; WT, 2.72 ± 0.65 ; $\text{prob}(\text{WT} > \text{5XFAD}) = 0.22$; *5XFAD*, $n = 153$ pyramidal cells, firing rate percentiles = 0, 0.47, 1.40, 4.50, 26.97; WT, $n = 168$ pyramidal cells, firing rate percentiles = 0, 0.64, 1.58, 3.63, 18.98; non-theta: *5XFAD*, 1.57 ± 0.42 ; WT, 1.72 ± 0.38 ; $\text{prob}(\text{WT} > \text{5XFAD}) = 0.73$; *5XFAD*, $n = 293$ pyramidal cells, firing rate percentiles = 0, 0.19, 0.55, 1.91, 24.79; WT, $n = 238$ pyramidal cells, firing rate percentiles = 0, 0.30, 0.85, 2.33, 10.88; theta: *5XFAD*, 1.73 ± 0.47 ; WT, 1.73 ± 0.47 ; $\text{prob}(\text{WT} > \text{5XFAD}) = 0.51$; *5XFAD*, $n = 284$ pyramidal cells, firing rate percentiles = 0, 0.20, 0.59, 2.20, 24.53; WT, $n = 234$ pyramidal cells, firing rate percentiles = 0, 0.30, 0.85, 2.16, 18.80. (Right) Firing rates of post-synaptic interneurons during time periods of interest. During ripples: *5XFAD*, 10.31 ± 3.54 ; WT, 9.30 ± 2.66 ; $\text{prob}(\text{WT} > \text{5XFAD}) = 0.36$; *5XFAD*, $n = 57$ interneurons, firing rate percentiles = 0, 3.00, 7.31, 15.45, 51.95; WT, $n = 63$ interneurons, firing rate percentiles = 0, 3.02, 7.99, 12.24, 46.12; non-theta: *5XFAD*, 8.00 ± 2.32 ; WT, 8.08 ± 2.49 ; $\text{prob}(\text{WT} > \text{5XFAD}) = 0.53$; *5XFAD*, $n = 83$ interneurons, firing rate percentiles = 0, 1.35, 4.60, 10.82, 42.16; WT, $n = 67$ interneurons, firing rate percentiles = 0, 2.77, 5.83, 10.80, 42.92; theta: *5XFAD*, 9.43 ± 2.14 ; WT, 10.29 ± 2.80 ; $\text{prob}(\text{WT} > \text{5XFAD}) = 0.71$; *5XFAD*, $n = 88$ interneurons, firing rate

percentiles = 0.029, 2.96, 6.63, 12.68, 37.76; WT, n = 68 interneurons, firing rate percentiles = 0, 3.46, 7.51, 14.95, 42.01.

See also Figures S2, S4, and S5. Black bar indicates median for violin plots. All percentiles are minimum, 25th percentile, median, 75th percentile, maximum. ⁺prob > 0.95 or prob < 0.05 ($\alpha = 0.10$). n.s., not significant throughout.

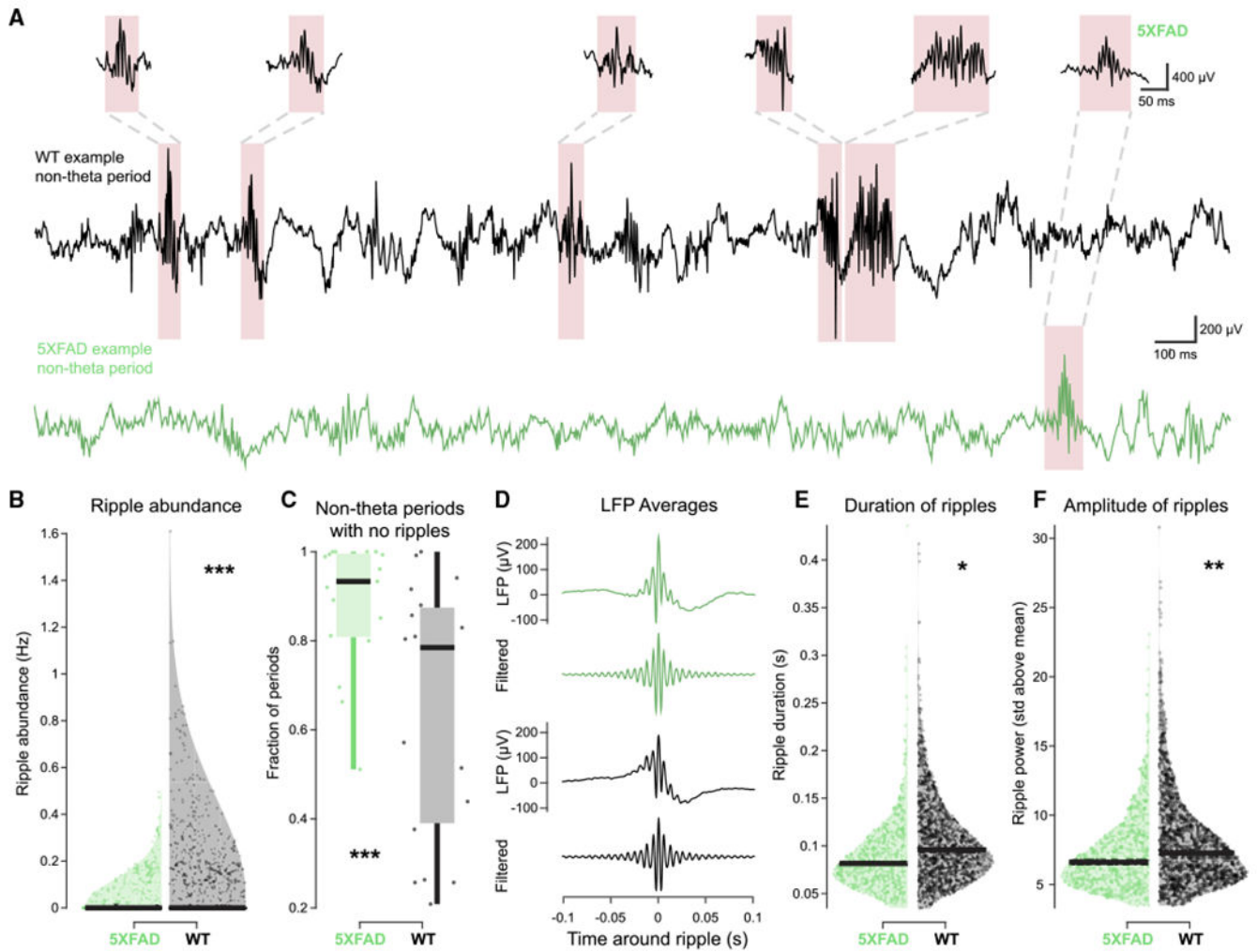


Figure 4. 5XFAD mice have shorter and fewer SWRs compared to WT mice

(A) Example non-theta periods with representative SWRs in 5XFAD (green) and WT (black) mice.

(B) Violin plot of SWR abundance during non-theta periods longer than 5 s in 5XFAD (green) versus WT (black) mice. Each dot indicates a non-theta period. Black bar at bottom indicates median. 5XFAD, 0.013 ± 0.0082 SWR abundance (Hz); WT, 0.074 ± 0.043 SWR abundance (Hz); $\text{prob}(\text{WT} > 5\text{XFAD}) = 0.9999$ (limit due to resampling 10^4 times)***; 5XFAD, $n = 1,969$ non-theta periods 5 s or longer, ripple abundance percentiles = 0, 0, 0, 0, 0.50; WT, $n = 1,389$ non-theta periods 5 s or longer, ripple abundance percentiles = 0, 0, 0, 0.08, 1.61 (minimum, 25th percentile, median, 75th percentile, maximum, respectively).

(C) Fraction of non-theta periods 5 s or longer with no SWRs in 5XFAD (green) and WT (black) mice. Each data point indicates a single recording session. Boxplot edges indicate quartiles, whiskers indicate range, and black bar indicates median. 5XFAD, 0.88 ± 0.053 proportion of periods; WT, 0.64 ± 0.098 proportion of periods; $\text{prob}(\text{WT} > 5\text{XFAD}) < 10^{-4}$ (limit due to resampling 10^4 times)***; 5XFAD, $n = 17$ sessions, fraction of periods with no ripples percentiles = 0.51, 0.81, 0.93, 0.99, 1; WT, $n = 19$ sessions, fraction of periods with no ripples percentiles = 0.21, 0.40, 0.78, 0.87, 1.

(D) Averages of all SWR events in *5XFAD* (green) and WT (black) mice aligned by peak of filtered signal. For green and black traces, top indicates LFP signal (1300 Hz) from the peak ripple power channel, and bottom indicates filtered LFP signal (150–250 Hz) from the peak ripple power channel.

(E) Distribution of SWR durations in *5XFAD* (green) versus WT (black) mice. Each dot indicates a SWR event. Black bar indicates median. SWRs had to be a minimum of 0.015 s above a threshold, so no SWRs are shorter than 0.015 s. *5XFAD*, 0.090 ± 0.0098 s; WT, 0.11 ± 0.0074 s; $\text{prob}(\text{WT} > \text{5XFAD}) = 0.9787^*$; *5XFAD*, $n = 776$ SWRs, ripple duration percentiles = 0.035, 0.065, 0.082, 0.11, 0.44; WT, $n = 1,542$ SWRs, ripple duration percentiles = -0.034, 0.074, 0.096, 0.13, 0.42.

(F) As in (E) for SWR power as measured in standard deviations (SD) above the SWR power mean. SWRs had to be a minimum of 3 SD above the mean, so no SWRs have less power than 3 SD. *5XFAD*, 7.29 ± 1.01 SD above the mean; WT, 8.18 ± 0.49 SD above the mean, $\text{prob}(\text{WT} > \text{5XFAD}) = 0.9977^{**}$; *5XFAD*, $n = 776$ SWRs, ripple power percentiles = 3.45, 5.35, 6.61, 8.48, 23.08; WT, $n = 1,542$ SWRs, ripple duration percentiles = 3.48, 5.71, 7.28, 9.53, 30.79.

See also Figure S6. All percentiles are minimum, 25th percentile, median, 75th percentile, maximum. * $\text{prob} > 0.975$ or $\text{prob} < 0.025$ ($\alpha = 0.05$); ** $\text{prob} > 0.995$ or $\text{prob} < 0.005$ ($\alpha = 0.01$); *** $\text{prob} > 0.9995$ or $\text{prob} < 0.0005$ ($\alpha = 0.001$) throughout.

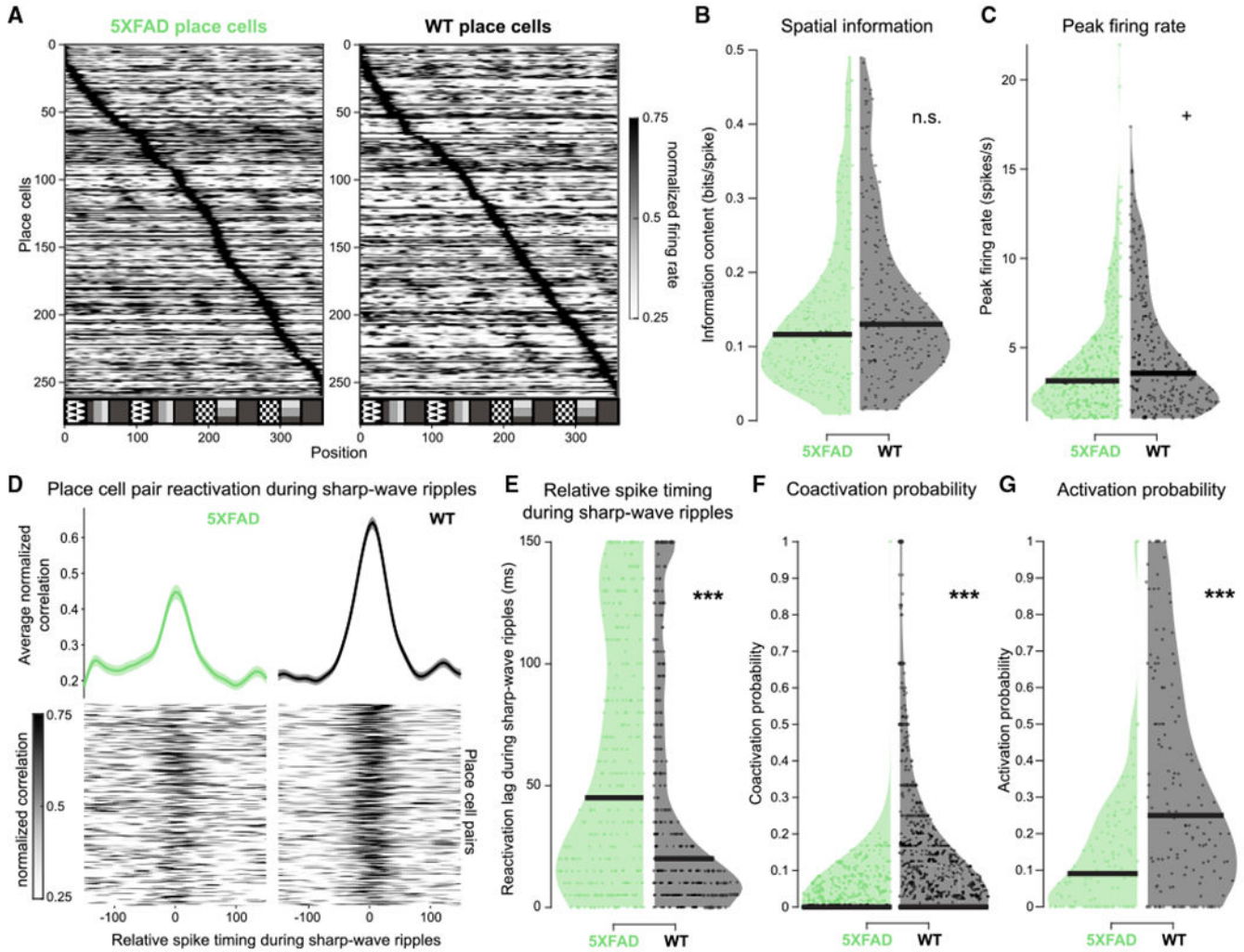


Figure 5. Place cells of *5XFAD* mice have lower probability of activation and coactivation during SWRs

(A) All place cells in *5XFAD* and WT mice, sorted by normalized peak firing rate.

(B) Distribution of spatial information of place cells with spatially tuned firing in this task in *5XFAD* (green) versus WT (black) mice. Each dot indicates a single place cell. *5XFAD*, 0.14 ± 0.016 bits/spike; WT, 0.16 ± 0.018 bits/spike; $\text{prob}(\text{WT} > \text{5XFAD}) = 0.94$; *5XFAD*, $n = 271$ place cells, spatial information percentiles = 0.0081, 0.068, 0.12, 0.18, 0.49; WT, $n = 215$, spatial information percentiles = 0.015, 0.082, 0.13, 0.21, 0.49 (min, 25th percentile, median, 75th percentile, and maximum, respectively). We observed some outliers, and so we removed them as described in STAR Methods.

(C) As in (B) for peak firing rate of place cells. *5XFAD*, 3.97 ± 0.52 Hz; WT, 4.61 ± 0.53 Hz; $\text{prob}(\text{WT} > \text{5XFAD}) = 0.96^+$; *5XFAD*, $n = 336$ place cells, firing rate percentiles = 1.01, 1.89, 3.14, 5.03, 21.95; WT, $n = 265$, firing rate percentiles = 1.03, 2.02, 3.56, 6.29, 17.37.

(D) Reactivation during SWR events of place cell pairs with spiking near in time during theta in *5XFAD* and WT mice. (Bottom) Heatmaps of normalized CCGs of place cell pairs during SWR with spiking near in time during theta (lower half of the activity index of all place cell pairs). (Top) Average of all place cell pair reactivation during SWR events with

spiking near in time during theta, mean \pm SEM. Activity index distributions: *5XFAD*, 0.37 ± 0.035 , $n = 335$ place cell pairs; WT, 0.28 ± 0.065 , $n = 387$ place cell pairs; $\text{prob}(\text{WT } 5XFAD) = 0.030$, bootstrap test.

(E) Relative spike timing during SWRs in place cells that spike near in time during theta in *5XFAD* (green) and WT (black) mice. Each dot indicates the peak reactivation lag of a single place cell pair across all SWR events. The number of spikes included in this figure was 107,276 in *5XFAD* mice and 131,910 in WT mice. *5XFAD*, 59.84 ± 7.37 ms; WT, 43.41 ± 5.77 ms; $\text{prob}(\text{WT } 5XFAD) = 0.0003^{***}$; *5XFAD*, $n = 335$ place cell pairs, spike timing lags during ripples percentiles = 0, 10, 45, 110, 150; WT, $n = 387$, spike timing lags during ripples percentiles = 0, 5, 20, 70, 150.

(F) SWR coactivation probabilities of place cells with spatially tuned firing in this task in *5XFAD* (green) versus WT (black) mice. Only animals with at least 10 SWRs during non-theta periods per recording were included. Each dot indicates the coactivation probability of a place cell pair across all SWR events. *5XFAD*, 0.024 ± 0.0049 probability; WT, 0.11 ± 0.025 probability; $\text{prob}(\text{WT } 5XFAD) > 0.9999$ (limit due to resampling 10^4 times) *** ; *5XFAD*, $n = 845$ place cell pairs, coactivation probability percentiles = 0, 0, 0, 0.026, 1; WT, $n = 1,061$ place cell pairs, coactivation probability percentiles = 0, 0, 0, 0.15, 1.

(G) As in (F) for SWR activation probabilities of place cells. *5XFAD*, 0.14 ± 0.035 probability; WT, 0.32 ± 0.049 probability; $\text{prob}(\text{WT } 5XFAD) > 0.9999$ (limit due to resampling 10^4 times) *** ; *5XFAD*, $n = 125$ place cells, activation probability percentiles = 0, 0, 0.091, 0.22, 1; WT, $n = 157$, activation probability percentiles = 0, 0.081, 0.25, 0.50, 1. See also Figure S7. Black bars indicate median of distribution for violin plots. All percentiles are minimum, 25th percentile, median, 75th percentile, maximum. $^{**}\text{prob} > 0.995$ or $\text{prob} < 0.005$ ($\alpha = 0.01$); $^{***}\text{prob} > 0.9995$ or $\text{prob} < 0.0005$ ($\alpha = 0.001$). n.s., not significant throughout.

Genotypes, recording sessions, single units, sharp-wave ripples, and putative monosynaptic connections per animal

Table 1.

Animal	Genotype	Breeding pair	Recording session	Total duration of recording sessions (min)	Single units	Sharp-wave ripples	Total duration of non-theta periods (min)	Monosynaptic connections (PYR-INT, INT-PYR)
F1	5XFAD	A	1	185.21	83	0	21.61	0, 0
F1	5XFAD	A	2	181.62	85	4	83.08	63, 21
F1	5XFAD	A	3	86.76	24	0	0	10, 0
F1	5XFAD	A	4	129.60	85	32	22.63	25, 18
F7	5XFAD	A	1	105.59	71	0	7.41	15, 4
F7	5XFAD	A	2	136.22	61	1	39.16	9, 9
F8	WT	A	1	104.99	7	45	15.40	0, 0
F8	WT	A	2	112.81	119	7	26.41	34, 18
F8	WT	A	3	124.14	20	392	24.08	13, 4
F8	WT	A	4	125.57	12	157	24.58	7, 3
F9	WT	B	1	123.23	33	83	5.30	0, 0
F9	WT	B	2	170.61	58	11	169.21	86, 59
F9	WT	B	3	164.45	43	23	154.14	16, 11
F9	WT	B	4	50.27	92	1	28.95	62, 21
F10	5XFAD	B	1	78.43	99	1	71.64	100, 57
F10	5XFAD	B	2	170.93	89	45	122.23	103, 45
F10	5XFAD	B	3	150.86	53	3	3.46	22, 15
F10	5XFAD	B	4	50.30	122	0	0.19	21, 6
F11	5XFAD	B	1	157.87	92	6	6.70	27, 6
F11	5XFAD	B	2	142.93	81	501	73.13	14, 6
F11	5XFAD	B	3	152.93	86	2	3.88	32, 13
F12	WT	B	1	146.18	110	113	8.25	43, 26
F12	WT	B	2	141.64	87	67	9.56	23, 3
F12	WT	B	3	98.61	30	24	17.45	25, 11
F12	WT	B	4	46.77	60	216	23.00	16, 6
F13	5XFAD	B	1	207.25	57	1	4.37	40, 26

Animal	Genotype	Breeding pair	Recording session	Total duration of recording sessions (min)	Single units	Sharp-wave ripples	Total duration of non-theta periods (min)	Monosynaptic connections (PYR-INT, INT-PYR)
F13	<i>5XFAD</i>	B	2	186.25	58	22	11.43	21, 10
F14	WT	B	1	153.42	141	74	38.65	71, 56
F14	WT	B	2	155.48	84	87	43.90	29, 11
F14	WT	B	3	50.20	53	8	2.33	6, 2
F15	WT	C	1	135.00	14	91	9.01	2, 2
F15	WT	C	2	126.71	10	135	21.38	2, 2
F16	<i>5XFAD</i>	C	1	161.75	90	15	80.00	51, 26
F16	<i>5XFAD</i>	C	2	75.71	85	87	24.43	0, 0
F18	<i>5XFAD</i>	C	1	94.89	12	40	25.93	7, 2
F19	<i>5XFAD</i>	D	1	96.52	30	16	28.39	10, 1
F20	WT	D	1	133.97	56	6	93.62	26, 14
F20	WT	D	2	95.88	24	1	1.08	6, 2
F20	WT	D	3	23.45	31	1	23.41	0, 0

KEY RESOURCES TABLE

REAGENT or RESOURCE	SOURCE	IDENTIFIER
Experimental models: organisms/strains		
Mouse: B6SJL-Tg(APPswFILon,PSEN1*M146L*L286V) 6799Vas/Mmjax	Jackson Laboratories	34840-JAX
Software and algorithms		
MATLAB	Mathworks Inc.	https://www.mathworks.com/
ViRMEn	Aronov and Tank, 2014	https://pni.princeton.edu/pni-software-tools/virmen
MountainSort	Chung et al., 2017	https://github.com/flatironinstitute/mountainsort

Author Manuscript

Author Manuscript

Author Manuscript

Author Manuscript